

Using Machine Learning with Partial Dependence Analysis to Investigate Coupling Between Soil Moisture and Near-surface Temperature

Jared T. Trok¹, Frances V. Davenport², Elizabeth A. Barnes², and Noah S. Diffenbaugh¹

¹Stanford University

²Colorado State University

April 4, 2023

Abstract

Soil moisture influences near-surface air temperature by partitioning downwelling radiation into latent and sensible heat fluxes, through which dry soils generally lead to higher temperatures. The strength of this coupled soil moisture-temperature (SM-T) relationship is not spatially uniform, and numerous methods have been developed to assess SM-T coupling strength across the globe. These methods tend to involve either idealized climate-model experiments or linear statistical methods which cannot fully capture nonlinear SM-T coupling. In this study, we propose a nonlinear machine learning-based approach for analyzing SM-T coupling and apply this method to various mid-latitude regions using historical reanalysis datasets. We first train convolutional neural networks (CNNs) to predict daily maximum near-surface air temperature (TMAX) given daily SM and geopotential height fields. We then use partial dependence analysis to isolate the average sensitivity of each CNN's TMAX prediction to the SM input under daily atmospheric conditions. The resulting SM-T relationships broadly agree with previous assessments of SM-T coupling strength. Over many regions, we find nonlinear relationships between the CNN's TMAX prediction and the SM input map. These nonlinearities suggest that the coupled interactions governing SM-T relationships vary under different SM conditions, but these variations are regionally dependent. We also apply this method to test the influence of SM memory on SM-T coupling and find that our results are consistent with previous studies. Although our study focuses specifically on local SM-T coupling, our machine learning-based method can be extended to investigate other coupled interactions within the climate system using observed or model-derived datasets.

1 **Using Machine Learning with Partial Dependence Analysis to Investigate Coupling**
2 **Between Soil Moisture and Near-surface Temperature**

3
4 **Jared T. Trok¹, Frances V. Davenport^{1,2,3}, Elizabeth A. Barnes², and Noah S.**
5 **Diffenbaugh^{1,4}**

6
7 ¹Department of Earth System Science, Stanford University, Stanford, CA, USA.

8 ²Department of Atmospheric Science, Colorado State University, Fort Collins, CO, USA

9 ³Department of Civil and Environmental Engineering, Colorado State University, Fort Collins,
10 CO, USA.

11 ⁴Doerr School of Sustainability, Stanford University, Stanford, CA, USA.

12
13 Corresponding author: Jared Trok (trok@stanford.edu)

14 **Key Points:**

- 15 • We investigate land-atmosphere interactions by applying machine learning techniques to
16 reanalysis datasets
- 17 • Partial dependence analysis reveals new insights into nonlinear summertime soil
18 moisture-temperature coupling and soil moisture memory
- 19 • These relationships broadly agree with previous studies, supporting machine learning as a
20 method for quantifying surface-atmosphere coupling
- 21

22 **Abstract**

23 Soil moisture influences near-surface air temperature by partitioning downwelling
24 radiation into latent and sensible heat fluxes, through which dry soils generally lead to higher
25 temperatures. The strength of this coupled soil moisture-temperature (SM-T) relationship is not
26 spatially uniform, and numerous methods have been developed to assess SM-T coupling strength
27 across the globe. These methods tend to involve either idealized climate-model experiments or
28 linear statistical methods which cannot fully capture nonlinear SM-T coupling. In this study, we
29 propose a nonlinear machine learning-based approach for analyzing SM-T coupling and apply
30 this method to various mid-latitude regions using historical reanalysis datasets. We first train
31 convolutional neural networks (CNNs) to predict daily maximum near-surface air temperature
32 (TMAX) given daily SM and geopotential height fields. We then use partial dependence analysis
33 to isolate the average sensitivity of each CNN's TMAX prediction to the SM input under daily
34 atmospheric conditions. The resulting SM-T relationships broadly agree with previous
35 assessments of SM-T coupling strength. Over many regions, we find nonlinear relationships
36 between the CNN's TMAX prediction and the SM input map. These nonlinearities suggest that
37 the coupled interactions governing SM-T relationships vary under different SM conditions, but
38 these variations are regionally dependent. We also apply this method to test the influence of SM
39 memory on SM-T coupling and find that our results are consistent with previous studies.
40 Although our study focuses specifically on local SM-T coupling, our machine learning-based
41 method can be extended to investigate other coupled interactions within the climate system using
42 observed or model-derived datasets.

43

44 **Plain Language Summary**

45 Soil moisture content influences air temperature by controlling evaporation at the soil
46 surface. Dry soils reduce evaporation which warms the surface and leads to higher air
47 temperatures. Conversely, wet soils generally lead to cooler temperatures. This process results in
48 a coupled relationship between soil moisture and temperature. Soil moisture-temperature (SM-T)
49 coupling occurs everywhere but is especially strong in certain areas of the world. Over recent
50 decades, numerous methods have been developed to measure regional differences in SM-T
51 coupling strength. These studies agree on certain "hot spots" where this coupling relationship is
52 particularly strong. However, these previous studies rely on idealized climate model experiments
53 or linear statistics which cannot fully capture nonlinear SM-T coupling. To address this, we
54 apply nonlinear machine learning techniques to investigate SM-T coupling. Our results show that
55 this method captures the nonlinear characteristics of SM-T coupling and agrees well with
56 previously documented coupling hot spots. Our method also provides a framework for using
57 machine learning to investigate other coupled processes in the Earth system.

58

59 **1 Introduction**

60 Since the early 1980's, climate model experiments have confirmed that soil moisture
61 content (SM) influences near-surface air temperature by modulating the surface energy budget
62 (Shukla & Mintz, 1982). This coupled relationship between soil moisture and temperature
63 (hereafter, "SM-T coupling") results from complex interactions between the land surface and the
64 atmosphere. In regions with strong SM-T coupling, SM content controls the partitioning of

65 downwelling radiation into latent and sensible heat fluxes, resulting in a positive feedback
66 mechanism through which dry soils lead to higher temperatures and further soil drying, while
67 wet soils generally lead to cooler temperatures (Seneviratne et al., 2010). Second-order positive
68 feedback mechanisms have also been observed between soil moisture, boundary layer growth,
69 1000–500-hPa thickness, and near-surface temperature (Fischer et al., 2007; Miralles et al.,
70 2014; Quesada et al., 2012; Seneviratne et al., 2010). These SM-T coupling mechanisms tend to
71 be strongest in transitional regimes between wet and dry climates, which is consistent with the
72 theoretical framework of Seneviratne et al., (2010). In wet and dry climate regimes, near-surface
73 temperature is less sensitive to SM (i.e., decoupled) since evapotranspiration is limited by
74 radiation and soil properties, respectively (Seneviratne et al., 2010). However, in transitional
75 climate regimes, near-surface temperature is highly sensitive to SM content because small
76 changes in SM influence evapotranspiration, which directly affects latent and sensible heat
77 fluxes (Seneviratne et al., 2010). Together with SM content, differences in soil characteristics
78 (e.g., albedo, porosity, texture) and land cover type also drive regional differences in SM-T
79 coupling strength (Dennis and Berbery 2021; Hirsch et al. 2014).

80 SM-T coupling has both local (Durre et al., 2000; J. Liu & Pu, 2019) and non-local (i.e.,
81 downwind) effects (Schwingshackl et al., 2018; Seneviratne et al., 2013; Vautard et al., 2007)
82 that occur on daily, monthly, and seasonal time scales (Durre et al., 2000; Fischer et al., 2007;
83 Koster et al., 2006a; J. Liu & Pu, 2019; Vautard et al., 2007). Deep soil layers (10-200 cm) have
84 longer SM memory (Wu & Dickinson, 2004), which makes these layers more important for
85 monthly- and seasonal-scale SM-T coupling (Koster et al., 2006a). In contrast, the uppermost
86 soil layer (< 10 cm) has the greatest influence on daily-scale SM-T coupling (J. Liu & Pu, 2019).
87 Further, the potential for SM-T coupling is highest during daylight hours in the summer months
88 (due in large part to the maximum of downwelling solar radiation; Durre et al., 2000; Koster et
89 al., 2006a; J. Liu & Pu, 2019), which makes daily-scale SM-T coupling especially relevant for
90 producing extreme daily maximum summer temperatures (Diffenbaugh et al., 2007; Miralles et
91 al., 2014; Schwingshackl et al., 2017; Seneviratne et al., 2010; Vogel et al. 2017). As a result, we
92 focus our analysis primarily on daily-scale coupling between top-layer SM and daily maximum
93 2-meter temperature in the summer months.

94 Over the past two decades, many studies have quantified regional differences in SM-T
95 coupling strength using observational (Chen et al., 2019; Dirmeyer, 2011; Koster et al., 2009;
96 Mei & Wang, 2012; Miralles et al., 2012; Spennemann et al., 2018; Teuling et al., 2009) and
97 model-derived datasets (Fischer et al., 2007; Jaeger et al., 2009; Koster et al., 2006a, 2009; Mei
98 & Wang, 2012; Ruscica et al., 2014; Schwingshackl et al., 2017; Seneviratne, Lüthi, et al.,
99 2006). Global assessments of SM-T coupling strength typically involve comparing climate
100 model simulations under different soil moisture scenarios (e.g., Fischer et al., 2007; Koster et al.,
101 2006a; Seneviratne, Lüthi, et al., 2006) or analyzing linear statistics (e.g., correlation
102 coefficients) between land-surface and/or atmospheric variables (e.g., Diffenbaugh & Ashfaq,
103 2010; Dirmeyer, 2011; Jaeger et al., 2009; Seneviratne, Lüthi, et al., 2006; Teuling et al., 2009).
104 Regardless of the methodology, previous assessments broadly agree on certain transitional
105 climate regimes as “hot spots” of SM-T coupling (e.g., the US Southern Great Plains, the Sahel
106 region in Africa, areas of the Indian subcontinent). However, these studies consistently disagree
107 on the relative magnitudes of SM-T coupling strength within certain regions. Inconsistencies
108 between SM-T coupling studies can result from numerous sources, including climate model
109 disagreement (Gevaert et al., 2018), model initializations (Fischer et al., 2007), experimental
110 design (e.g., potential sea surface temperature effects; Koster et al., 2006a), and differences

111 between climate model and reanalysis datasets (e.g., stronger SM-evaporative fraction coupling
112 in reanalysis compared to climate models; Mei & Wang, 2012). In climate model-based
113 assessments of SM-T coupling, additional inconsistencies can be caused by differences in model
114 parameterization of soil hydraulic properties, plant hydraulic properties, vegetation type, and
115 land use (Dennis and Berbery 2021; Hirsch et al. 2014).

116 Importantly, analyses of SM-T coupling strength (e.g., Dirmeyer, 2011; Fischer et al.,
117 2007; Jaeger et al., 2009; Koster et al., 2006a; Menendez et al., 2019; Miralles et al., 2012;
118 Ruscica et al., 2014; Seneviratne, Lüthi, et al., 2006; Teuling et al., 2009) have tended to use
119 idealized climate model experiments and/or linear statistical methods to explain SM-T coupling.
120 However, evidence suggests that the sensitivity of temperature to SM changes for different
121 values of SM (Benson & Dirmeyer, 2021; Jaeger & Seneviratne, 2011; Seneviratne et al., 2010).
122 This nonlinear relationship between temperature and SM is difficult to estimate using climate
123 model experiments, requiring a large number of sensitivity experiments with slightly perturbed
124 SM conditions repeated over numerous different atmospheric initializations (Fischer et al., 2007;
125 Seneviratne et al., 2010). There is thus an opening for nonlinear statistical methods that can
126 comprehensively assess SM-T coupling relationships without requiring extensive climate model
127 simulations.

128 Deep neural networks have recently surged in popularity for their ability to learn complex
129 nonlinear interactions between input and output variables (LeCun et al., 2015). Convolutional
130 neural networks (CNNs) are one particular form of deep learning architecture that are designed
131 to analyze gridded input data such as images and geospatial data (LeCun et al., 1989). To date,
132 CNNs have been used extensively in the geosciences for image classification (Chilson et al.,
133 2019; Davenport & Duffenbaugh, 2021; Jergensen et al., 2019; Lagerquist et al., 2019; Y. Liu et
134 al., 2016; Wang et al., 2016; Wimmers et al., 2019), model parameterization (Bolton & Zanna,
135 2019; Han et al., 2020; Larraondo et al., 2019; Pan et al., 2019), and forecasting (Ham et al.,
136 2019; Jacques-Dumas et al., 2021) applications. CNN models contain thousands (or millions) of
137 trainable weights which are optimized during the training process to ensure that the CNN's
138 output predictions closely resemble the target data. In addition, these CNN models utilize
139 nonlinear mathematical functions to represent the complex nonlinear relationships between the
140 geospatial input maps and output predictions. After the training process is complete, machine-
141 learning (ML) model interpretation and visualization methods can be used to aid in interpreting
142 the predictions of trained CNNs (e.g., layer-wise relevance propagation, S. Bach et al., 2015;
143 backward optimization, Olah et al., 2017; etc.). These ML interpretation methods have been
144 used in the geosciences to confirm that a model's predictions are based on the inputs in a
145 physically meaningful way (Davenport & Duffenbaugh, 2021; Duffenbaugh & Barnes, 2023;
146 Gagne et al., 2019; McGovern et al., 2019). More recently, studies have also begun to use ML
147 interpretation methods to gain new insights into physical processes (Barnes, Mayer, et al., 2020;
148 Barnes, Toms, et al., 2020; Toms et al., 2020; Zhang et al., 2021).

149 Although applications of ML interpretation techniques are increasingly commonplace in
150 the geosciences, these techniques have the potential to give non-physical and/or misleading
151 results (Mamalakis et al. 2022; Ebert-Uphoff and Hilburn 2020). Typically, the results of ML
152 interpretation methods are deemed trustworthy by visually comparing results against prior
153 knowledge. This works well in cases where the processes are well understood and a ground-truth
154 comparison is available (Davenport & Duffenbaugh, 2021; Gagne et al., 2019; McGovern et al.,
155 2019). However, it remains difficult to validate ML interpretation results when investigating new

156 or poorly understood processes. Recently, the construction of synthetic benchmark datasets
 157 where the discoverable relationships are known a priori have been proposed as a way to assess
 158 the fidelity of ML interpretation results (Ebert-Uphoff & Hilburn, 2020; Mamalakis et al., 2022).
 159 Here, we show that by applying ML interpretation techniques to modified versions of our
 160 training dataset we can validate our results and gain additional insights into physical processes.

161 Partial dependence plots (PDPs; Friedman, 2001) are a common ML interpretation
 162 technique which can be used to visualize the nonlinear relationships that a model has learned
 163 between the input and output variables (Goldstein et al., 2015; Jergensen et al., 2019; McGovern
 164 et al., 2019). However, PDPs are rarely used to analyze deep-learning architectures (such as
 165 CNNs) for geoscience applications (Zhang et al., 2021). PDPs are infeasible for most deep-
 166 learning applications (especially those with a large number of inputs) because they require an
 167 assumption of independence between all input variables (McGovern et al., 2019). If variables are
 168 strongly correlated, certain combinations of input variables will not likely occur in nature, and
 169 the CNN will be forced to extrapolate beyond the training dataset in order to calculate the PDP
 170 (which can yield non-physical results). Additionally, in order to apply PDPs to CNNs we must
 171 have a physically meaningful way to sort geospatial input maps along a continuous axis (which
 172 can be difficult depending on the application). In spite of these limitations, PDPs show promise
 173 as a tool for analyzing CNNs to better understand complex nonlinear relationships within
 174 geospatial datasets, provided that the input variables are not too strongly correlated, and that the
 175 application is focused on quantifying the relationship between the output prediction and some
 176 quantity calculated from the input maps.

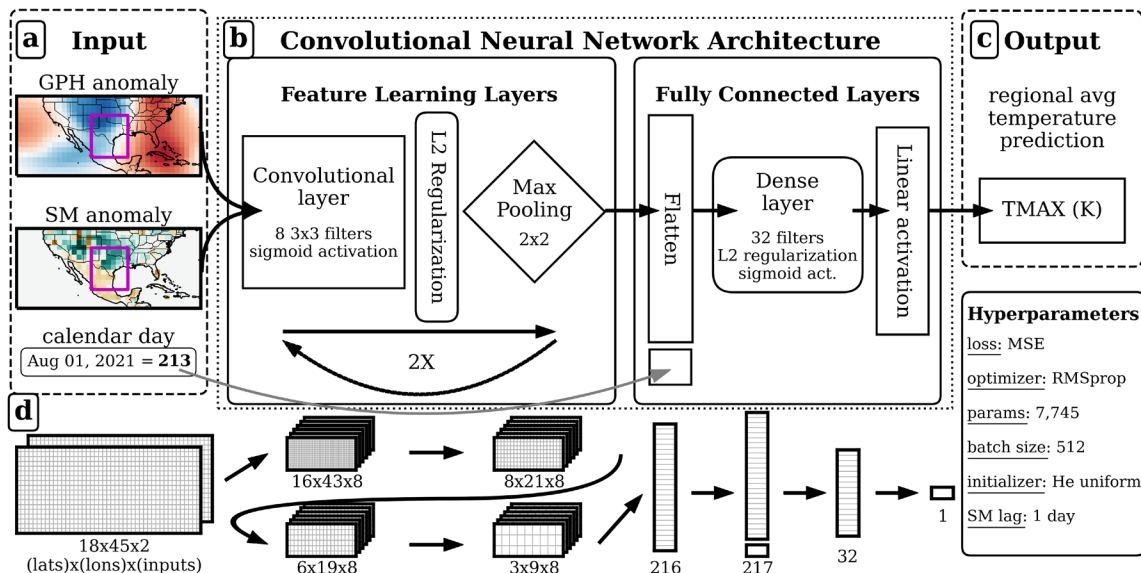


Figure 1. Schematic of the convolutional neural networks used in this analysis. (a) Model is given the following inputs: 500 millibar geopotential height (GPH) anomaly map, 0-7 cm volumetric soil moisture (SM) fraction anomaly map, and an integer input corresponding to the calendar day (normalized to fall between 0 and 1). Pink box shows the temperature prediction region. (b) The spatial input maps undergo feature learning as they are passed through a convolutional layer with 8 3x3 filters using sigmoid activation, followed by an L2 regularization layer (to reduce overfitting), and a 2x2 max pooling layer. These three feature learning layers repeat twice. The output from the feature learning layers is then flattened, and the normalized calendar day input is concatenated onto the end. The flattened vector is passed through a fully-connected dense layer with 32 neurons, L2 regularization, and sigmoid activation. Lastly, we use a linear activation function which outputs (c) the predicted TMAX. (d) The input and output size of each layer in the convolutional neural network. (e) Several hyperparameters used to construct and train each model.

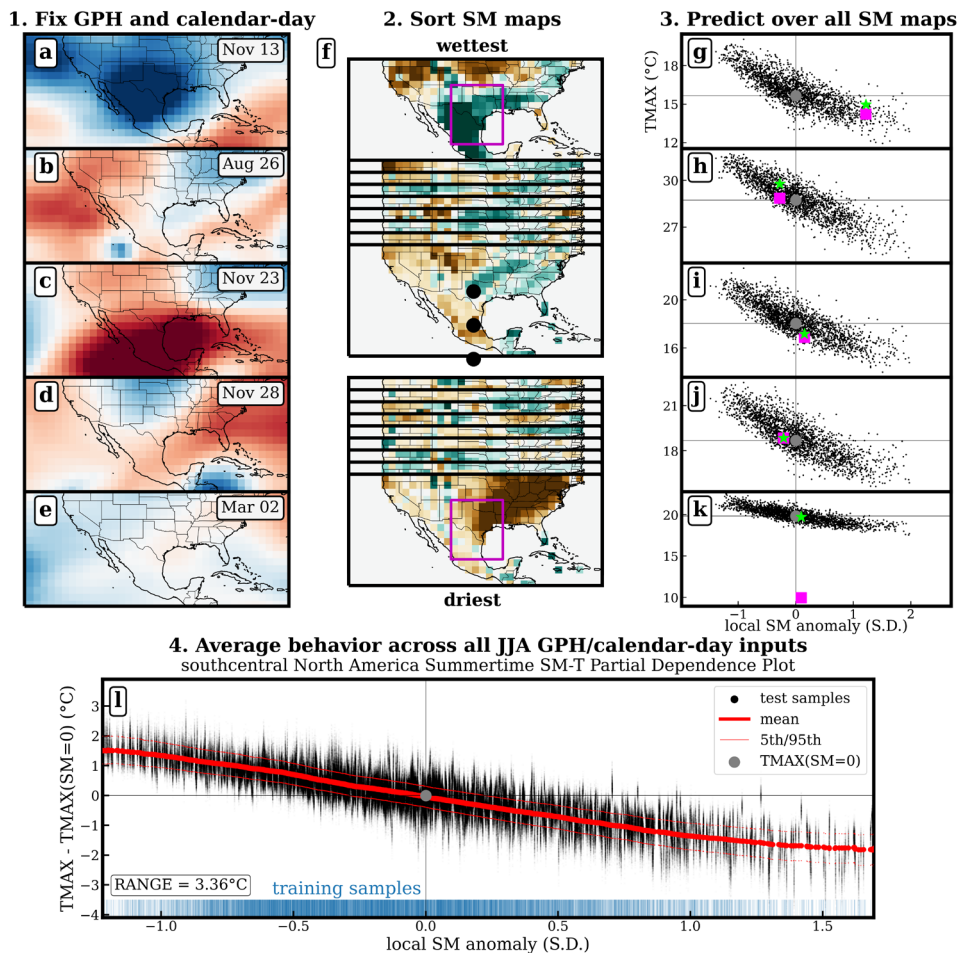


Figure 2. Schematic showing how partial dependence analysis is used to derive the nonlinear soil moisture-temperature coupling relationship that the convolutional neural network has learned through the training process. Shown is an example from a region in southcentral North America. (1) We take a single 500 millibar geopotential height map and the calendar day on which that map occurs. (2) We then pair this single GPH/calendar-day combination with every possible soil moisture anomaly input map (in the testing dataset) sorted from driest-wetttest (f) according to local SM anomaly (area-weighted average of all non-ocean grid cells inside the pink box). (3) We then pass these new input combinations through a trained convolutional neural network to obtain daily maximum temperature (TMAX) predictions for a single GPH/calendar-day combination over the entire range of SM anomaly maps. (4) We repeat steps (1)-(3) and average the behavior across all summertime GPH/calendar-day combinations (in the 8-year testing dataset) to obtain the nonlinear soil moisture-temperature coupling relationship (l) that the convolutional neural network has learned through the training process. The 5 GPH/calendar-day examples (a-e) are chosen for lowest GPH anomaly, median GPH anomaly, highest GPH anomaly, model best-hit, and model worst-miss, respectively. The corresponding temperature predictions for these 5 examples are given in (g)-(k). The pink marker in (g)-(k) indicates the actual ERA5-Land temperature that occurred on that particular day. The green marker in (g)-(k) shows the model predicted temperature. The black marker in (g)-(k) shows the average model prediction for SM anomalies near zero, or TMAX(SM=0). Model predictions for each GPH/calendar-day combination in the testing dataset are shifted by TMAX(SM=0), then averaged to obtain the SM-T relationship in (l). We also include a rug plot showing the distribution of SM anomalies in the training dataset. Soil moisture anomalies are calculated as standard deviations (S.D.) from the calendar-day mean.

178

179

180

181

182

183

184

In this study, we apply partial dependence analysis to investigate daily-scale nonlinear SM-T coupling relationships over sixteen midlatitude regions in the Northern and Southern Hemispheres. Over each prediction region, we train a CNN to predict daily maximum temperature using several input variables, including atmospheric pressure patterns and soil moisture (Figure 1). Next, we use partial dependence plots (PDPs) to visualize how the CNN's temperature prediction changes as we vary the SM input (while holding all other inputs constant;

185 Figure 2). The resulting SM-T PDP shows the average sensitivity of the CNN's daily
186 temperature prediction to the SM input. To ensure that these SM-T relationships are robust, we
187 confirm that each CNN meets minimum performance criteria and compare our SM-T PDPs
188 against those obtained from modified versions of our training datasets where we systematically
189 reduce and/or eliminate the potential for SM-T coupling.

190

191 **2 Data and Methods**

192 **2.1 Datasets**

193 We construct two neural network training datasets which use daily mean 500-hPa
194 geopotential height (GPH) anomalies and daily mean surface-layer volumetric soil moisture
195 fraction (SM) anomalies as predictors of regional average daily maximum 2-meter air
196 temperature (TMAX) over the 1979-2021 period. We focus on daily TMAX (as opposed to daily
197 minimum or daily mean temperature) because the coupling between surface-layer SM and 2-
198 meter temperature is most relevant during daylight hours (when SM controls the partitioning of
199 downwelling solar radiation into sensible and latent heat fluxes).

200 Our primary dataset consists of GPH, SM, and TMAX from the ERA5/ERA5-Land
201 historical reanalysis (ERA5, Hersbach et al., 2018; ERA5-Land, Muñoz-Sabater et al., 2021)
202 provided by the European Centre for Medium-Range Weather Forecasts and downloaded from
203 the Copernicus Climate Change Service Climate Data Store. We use ERA5 hourly 500-hPa
204 geopotential provided globally at $0.25^{\circ} \times 0.25^{\circ}$ horizontal resolution. We then divide the
205 geopotential by Earth's gravitational acceleration (9.80665 m s^{-2}) to obtain hourly 500-hPa GPH
206 fields in meters above mean sea level. We use ERA5-Land hourly 0-7 cm SM fraction and
207 hourly 2-meter air temperature provided globally at $0.1^{\circ} \times 0.1^{\circ}$ horizontal resolution. We then
208 aggregate the ERA5/ERA5-Land hourly fields to obtain daily mean GPH, daily mean SM, and
209 daily TMAX. Lastly, we convert the ERA5 GPH and SM fields to a T62 gaussian grid at
210 $1.875^{\circ} \times 1.875^{\circ}$ horizontal resolution to match the resolution of our comparison dataset, and to
211 reduce computational expense.

212 Our comparison dataset (used in supplemental analysis) consists of GPH, SM, and
213 TMAX from the NCEP/DOE Reanalysis II (NCEP; Kanamitsu et al., 2002) historical reanalysis
214 downloaded from the NOAA Physical Science Laboratory data archive at <https://psl.noaa.gov>.
215 Daily mean 0-10 cm SM fraction and daily 2-meter TMAX are available globally on a T62
216 gaussian grid at $1.875^{\circ} \times 1.875^{\circ}$ horizontal resolution. Using bilinear interpolation, we convert the
217 NCEP daily mean 500-hPa GPH fields from a $2.5^{\circ} \times 2.5^{\circ}$ rectangular grid to the T62 gaussian
218 grid to match the SM and TMAX fields (regridding performed using NetCDF Operators; Zender,
219 2008).

220 Since this analysis focuses on land-atmosphere interactions at daily timescales, we first
221 subtract the 1979-2021 area-weighted regional-mean linear trends from the GPH, SM, and
222 TMAX fields in both datasets (Cattiaux et al., 2013). By subtracting spatially averaged trends,
223 we avoid the impacts of uniform tropospheric thermal expansion and near-surface warming on
224 our training datasets, while still preserving the non-uniform spatial trends in GPH and SM that
225 are important drivers of regional TMAX (Horton et al., 2015; Swain et al., 2016). For both
226 ERA5 and NCEP, we then use the daily mean GPH and SM maps to calculate daily standardized
227 anomalies (i.e., z-scores) by subtracting grid-cell calendar-day means and dividing by grid-cell

228 calendar-day standard deviations. All missing SM values (non-land grid cells) are assigned a
 229 zero anomaly to avoid numerical issues with missing values during neural network training.

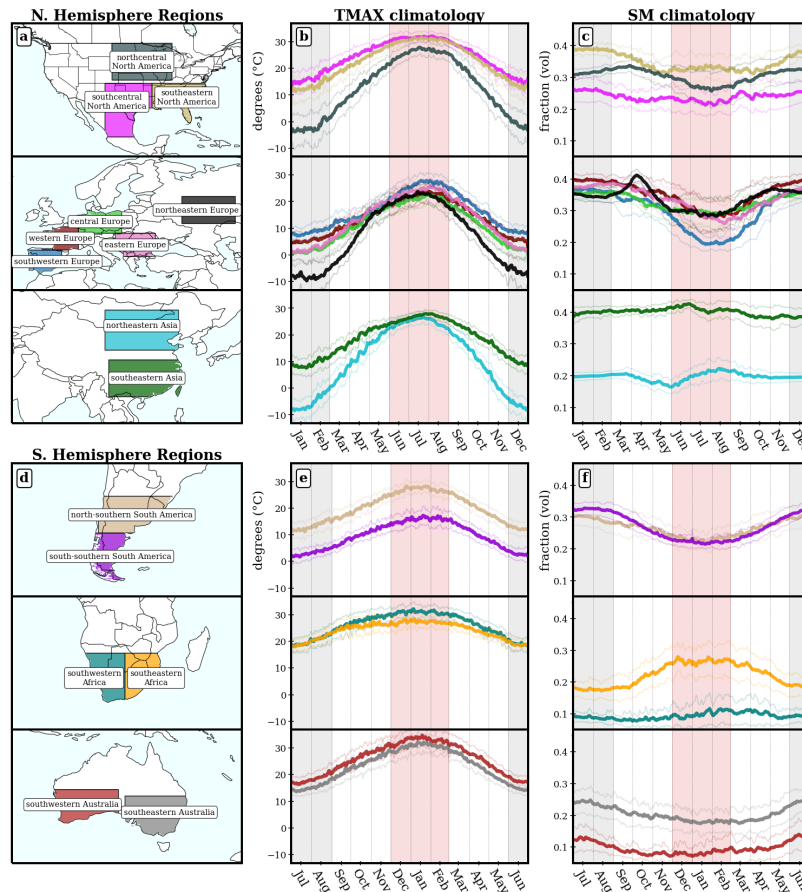


Figure 3. (a) Northern Hemisphere regions included in this analysis alongside 1979-2021 regional climatologies of (b) daily maximum 2-meter temperature (TMAX), and (c) volumetric soil moisture fraction (SM). (d, e, f) Same as (a, b, c) but for Southern Hemisphere regions. Red shading indicates summer months in each hemisphere over which this study analyzes soil moisture-temperature coupling. Gray shading indicates winter months removed from all subsequent analyses. Thin colored lines show ± 1 standard deviation. TMAX and SM climatologies derived from ERA5-Land dataset.

230

231 2.2 Regions

232 We define sixteen prediction regions chosen to encompass a wide range of mid-latitude
 233 climate regimes, including known land-atmosphere coupling “hot spots” (as proposed by, e.g.,
 234 Fischer et al., 2007; Koster et al., 2006b; Mei & Wang, 2012; Seneviratne, Lüthi, et al., 2006).
 235 The sixteen midlatitude regions (Figure 3) are: northcentral North America (38°N-49°N, 86°W-
 236 104°W), southcentral North America (21°N-37°N, 92°W-106°W), southeastern North America
 237 (25°N-37°N, 75°W-92°W), southwestern Europe (36°N-43°N, 10°W-1°E), western Europe
 238 (43°N-50°N, 5°W-6°E), central Europe (48°N-55°N, 6°E-19°E), eastern Europe (41°N-48°N,
 239 17°E-29°E), northeastern Europe (51°N-59°N, 37°E-53°E), northeastern Asia (36°N-48°N,
 240 99°E-121°E), southeastern Asia (22°N-33°N, 100°E-122°E), north-southern South America
 241 (30°S-41°S, 51°W-73°W), south-southern South America (41°S-55°S, 63°W-76°W),
 242 southwestern Africa (20°S-35°S, 12°E-25°E), southeastern Africa (20°S-35°S, 25°E-36°E),
 243 southwestern Australia (25°S-36°S, 112°E-133°E), and southeastern Australia (27°S-39°S,

244 135°E-154°E). The extent of the prediction regions (roughly 800-1100 km across) is determined
245 based on the approximate size of mid-latitude weather patterns.

246 Over each of these prediction regions (Figure 3), we construct neural network training
247 datasets (as detailed in Section 2.1). Each regional CNN uses standardized GPH and SM
248 anomaly maps as predictors of regional average TMAX. We calculate regional average TMAX
249 by taking an area-weighted mean over all non-ocean grid cells that fall within the region bounds.
250 In order to provide sufficient spatial context for each regional TMAX prediction, we use broad
251 GPH and SM anomaly input maps of 45 longitude points \times 18 latitude points (at $1.875^\circ \times 1.875^\circ$
252 horizontal resolution), centered around the prediction region (see Figure 1 for an example of
253 these input maps). Our choice of CNN input size (i.e., 45 longitude points \times 18 latitude points) is
254 based on the approach of Davenport and Diffenbaugh (2021), who showed that a CNN input map
255 extending 35 degrees latitudinally and 85 degrees longitudinally provides sufficient spatial
256 context for classifying GPH patterns associated with extreme precipitation over a similarly sized
257 mid-latitude prediction region in the US Midwest.

258

259 2.3 Convolutional Neural Network (CNN) Architecture

260 We train a separate CNN regression model (Figure 1) to predict average daily TMAX
261 over each prediction region using daily 500-hPa GPH anomalies, daily surface-layer SM
262 anomalies, and calendar-day inputs. For each day in the training set, the neural network receives
263 the calendar day (normalized to fall between 0 and 1) and a 3-dimensional spatial input matrix
264 ($18 \times 45 \times 2$; lat \times lon \times inputs) containing the GPH map from the day of the prediction and the SM
265 anomaly map from 1 day prior to prediction. We use SM inputs from 1 day prior to the
266 prediction in order to avoid potential impacts of daily TMAX on daily SM. The spatial inputs
267 then undergo feature learning as they are passed through two convolutional layers (8 3×3 filters
268 with sigmoid activation) each followed by a 2×2 max pooling layer. After feature learning, the
269 resulting feature maps are flattened into a 1-dimensional vector and the normalized calendar-day
270 input is concatenated to the end. This vector is then passed through a fully-connected (dense)
271 layer (32 neurons with sigmoid activations) followed by a final dense layer with linear
272 activations which output a single TMAX prediction. The TMAX predictions are then compared
273 to the target TMAX values from the training dataset, and CNN layer weights (initialized with He
274 uniform; He et al., 2015) are adjusted using RMSprop (Hinton, Srivastava, & Swersky, 2012) in
275 order to minimize the loss function (mean squared error; MSE). To reduce overfitting during the
276 training process, we use L2 activity regularization on both convolutional layers and the dense
277 layer. We also use early stopping with a patience threshold of 100 epochs which halts the
278 training process and returns the optimal weights when validation loss stops improving. After the
279 training process is complete, we save the model weights and use the trained model to predict
280 TMAX over all days.

281 Prior to neural network training, we randomly split the 43-year datasets into training (27-
282 year), validation (8-year), and testing (8-year) subsets while keeping calendar years intact. By
283 keeping calendar years intact, we further reduce the potential for overfitting between
284 chronologically adjacent days in different subsets which may look nearly identical due to slow
285 day-to-day variations in SM, GPH, and TMAX. Each subset consists of randomly selected years
286 (instead of a consecutive N-year period) to avoid potential impacts of interdecadal climate
287 variability, land use change, anthropogenic climate forcing, and trends in land-atmosphere

288 interactions which could otherwise prevent a fair evaluation of our model. We use different
289 training/validation/testing subsets for each region in order to ensure that the target TMAX
290 distributions are roughly equivalent between each subset. To avoid potential impacts of snow
291 cover on land-atmosphere coupling (Dutra et al., 2011; Henderson et al., 2018), we remove the
292 three canonical winter months in each hemisphere (December-January-February in the Northern
293 Hemisphere and June-July-August in the Southern Hemisphere). This yields a total of 7425
294 training samples, 2200 validation samples, and 2200 testing samples for each Northern
295 Hemisphere region; and 7378 training samples, 2186 validation samples, and 2186 testing
296 samples for each Southern Hemisphere region. During training, model parameters are fit to the
297 training data and hyperparameters are adjusted to minimize loss on the validation data. Once the
298 training is complete, we predict TMAX on the unseen testing subset.

299 We optimize CNN architecture and hyperparameters using scikit-learn's GridSearchCV
300 (Pedregosa et al., 2011), including: layer number/organization, filter number/size, loss function,
301 optimizer, activation functions, weight initializers, and batch size. Additional hyperparameters
302 such as initial learning rate, learning rate decay, and L2 activity regularization factor are
303 optimized separately for each regional model in order to minimize loss on the validation subset.
304 Due to the non-uniform nature of TMAX distributions, we use the DenseWeight/DenseLoss
305 algorithm (Steininger et al., 2021) to perform imbalanced regression by weighting the loss
306 function for each sample using weights inversely proportional to sample frequencies (calculated
307 via kernel density estimation). The DenseWeight hyperparameter (which controls the degree of
308 weighting) is optimized separately for each regional CNN and substantially improves model
309 performance on extreme TMAX days. Although sinusoidal-based positional encoding is
310 commonly used to encode temporal cycles as a CNN input variable, this method forces a
311 seasonal symmetry in the input data. Given that a region's seasonal cycle of TMAX and SM are
312 not symmetric (e.g., Figure 3), we instead use a normalized calendar-day integer input for this
313 prediction task. We use Tensorflow with Keras 2.7.0 (Tensorflow Developers, 2021) to construct
314 and train each model.

315

316 2.4 Evaluating CNN Performance

317 Prior to using the regional CNNs to quantify SM-T coupling strength, we must first
318 evaluate whether the CNNs are sufficiently accurate to represent SM-T coupling at daily
319 timescales over the respective regions. To that end, we first ensure that each CNN meets two
320 criteria: (1) the CNN accurately predicts TMAX at daily timescales, and (2) the SM input
321 contributes substantially to overall CNN performance at daily timescales.

322 To determine if a CNN meets these criteria for a given region, we compare the
323 performance of our CNN against two model performance baselines:

- 324 a. Seasonal climatology: comparison between the calendar-day mean TMAX and
325 the actual daily TMAX on individual calendar days;
- 326 b. CNN without SM input: performance of a CNN model trained with GPH and
327 calendar-day inputs but no SM input maps.

328 We first compare the performance metrics (e.g., R^2 , MAE, MSE) of our CNNs with those
329 of the seasonal-climatology baseline. Any model which outperforms the seasonal-climatology
330 baseline should, to some degree, be able to predict daily TMAX anomalies from the seasonal

331 cycle. Then, to justify whether the SM input contributes to overall model skill at daily
332 timescales, we compare the performance of our CNNs with all input variables against the CNN-
333 without-SM baseline. The difference in skill between these models helps to quantify how much
334 the SM input contributes to overall model skill at daily timescales. If the CNN with all input
335 variables outperforms the CNN-without-SM baseline, and both of these CNN models outperform
336 the seasonal-climatology baseline, then we can more confidently use the full CNN to assess SM-
337 T coupling at daily timescales.

338

339 2.5 Evaluating Coupling Strength Using Partial Dependence

340 After training and evaluating our CNNs, we apply partial dependence analysis (Figure 2;
341 Friedman, 2001) to visualize the nonlinear relationships between each CNN's summertime
342 TMAX predictions and the average local SM anomaly calculated from the SM input maps.
343 Although the training datasets include data from all nine non-winter months in each hemisphere,
344 we only assess SM-T coupling over the three canonical summer months (when the potential for
345 SM-T coupling is highest; Koster et al., 2006b). First, we select a single GPH anomaly map and
346 the corresponding calendar-day input from a summer day in the testing dataset (Figure 2a-e).
347 Holding this GPH and calendar-day input constant, we pair these fixed inputs with every daily
348 SM map (in the testing dataset) sorted from driest to wettest according to the prediction region's
349 average SM anomaly (area-weighted mean over all non-ocean grid cells; Figure 2f). Then, we
350 use each trained CNN to predict TMAX from these newly constructed input combinations and
351 visualize the results to assess how the CNN's TMAX prediction depends on the average local
352 SM anomaly under daily GPH conditions (Figure 2g-k). We repeat this process for all summer
353 days in the testing dataset (8 years) and compute the two-sided moving average (200 points on
354 either side) to obtain the smoothed regional summertime SM-T partial dependence plot (PDP)
355 that the CNN has learned through the training process (Figure 2l). Our two-sided moving
356 average is calculated using smaller window sizes near the extreme SM anomalies to ensure an
357 equal number of points on each side. We also remove the 10 driest and 10 wettest SM anomaly
358 maps (in the testing dataset) from the PDP calculation in order to avoid biasing the results at
359 extreme SM anomalies that are underrepresented in the training dataset. Areas of the PDP plot
360 with non-zero SM-T PDP slope indicate where the CNN's TMAX prediction is sensitive to the
361 local SM anomaly calculated from the SM input map (McGovern et al., 2019). We also use the
362 vertical extent (range) of our SM-T PDPs as a relative indicator of SM-T coupling strength.

363 In order to compare the effects of SM anomalies across different days, we compute PDPs
364 using centered TMAX predictions (Goldstein et al., 2015). For each day, we calculate the change
365 in TMAX relative to the model's average prediction near climatological SM conditions (i.e.,
366 $TMAX(SM=0)$). We estimate $TMAX(SM=0)$ each day by averaging the closest 200 daily
367 predictions that fall on either side of the calendar-day mean SM anomaly (i.e., $SM=0$).
368 Estimation of $TMAX(SM=0)$ is largely insensitive to the choice of window size (i.e., 200
369 predictions on either side).

370 Because partial dependence analysis also relies on the assumption that all input variables
371 are independent from one another (Friedman, 2001), we use SM and GPH calendar-day
372 anomalies to remove seasonal variability. However, there still remains the potential for
373 interaction effects between SM and GPH which may cause the CNN to learn different SM-T
374 relationships for different GPH inputs. In this case, SM-T PDP curves can be misleading since

375 they would average out these divergent SM-T relationships. We address this issue by including
376 density plots of daily TMAX predictions alongside the PDPs. From these density plots, we can
377 confirm that the PDPs are not averaging out divergent SM-T relationships caused by a violation
378 of the independence assumption between SM and GPH inputs (Goldstein et al., 2015).

379 To assess the fidelity of our PDP-based approach, we apply the PDP method (Figure 2) to
380 modified versions of our training datasets (i.e., baseline datasets) in which we have eliminated
381 the potential for SM-T coupling. We construct a single baseline dataset by randomly shuffling
382 the 1979-2021 daily SM input maps while leaving the GPH and calendar-day inputs untouched.
383 Then, we train a new CNN using this baseline dataset, save the model weights, and apply the
384 PDP method to obtain a baseline SM-T relationship. We repeat this process for numerous
385 baseline datasets, each created with a different random seed. Randomizing the SM maps removes
386 any statistical link between SM inputs and TMAX outputs within these baseline datasets.
387 Therefore, we expect each baseline SM-T relationship to have zero slope. Using an approach
388 similar to Buja et al., (2009) and Wickham et al. (2010), we then compare the true PDPs against
389 100 baseline PDPs (each obtained from a different baseline dataset) to determine whether the
390 true PDP exhibits a relationship with SM beyond that of random noise.

391

392 **3 Results**

393 We show TMAX and SM climatologies calculated from the ERA5-Land dataset (1979-
394 2021) for each of the sixteen mid-latitude regions (Figure 3). All sixteen regions experience their
395 highest temperatures during the summer months and lowest temperatures during the winter
396 months (Figures 3b and 3e). However, there are large regional differences in the magnitude of
397 the TMAX seasonal cycle, ranging from $\pm 10^{\circ}\text{C}$ in southwestern Africa and southeastern Africa
398 to $\pm 35^{\circ}\text{C}$ in northeastern Europe and northeastern Asia. Although SM seasonal cycles differ
399 substantially between regions, nearly all regions experience their driest SM conditions in the
400 summer months (with the exception of northeastern Asia, southeastern Asia, southwestern
401 Africa, and southeastern Africa; Figures 3c and 3f). For most regions, we find that the TMAX
402 and SM climatologies also show these patterns in the NCEP/DOE Reanalysis II dataset (Figure
403 S5). (See Methods for additional information about region selection.)

404

405 **3.1 CNN Model Evaluation**

406 For each region, we compare the performance of our CNN regression models against two
407 model performance baselines (detailed in Section 2.4; Figures 4-6). Across all regions, the CNN-
408 without-SM baselines outperform the seasonal-climatology baseline (i.e., Figures 4-6(b) vs.
409 Figures 4-6(c)), ranging from a minimum RMSE reduction of 10.4% in southeastern Asia to a
410 maximum RMSE reduction of 50.7% in southwestern Europe. We also find that our CNN
411 models with all input variables (including SM inputs) outperform the CNN-without-SM
412 baselines (i.e., Figures 4-6(a) vs. Figures 4-6(b)), ranging from a minimum RMSE reduction of
413 8.1% in northcentral North America to a maximum RMSE reduction of 24.8% in southwestern
414 Africa. These improvements in CNN model skill indicate that both GPH inputs and SM inputs
415 each provide unique information that is useful for predicting TMAX at daily timescales.
416 Therefore, we find that all regional CNNs satisfy the necessary criteria (detailed in Section 2.4)
417 to confidently use partial dependence analysis to assess daily-scale SM-T coupling. (We further

418 analyze each CNN's ability to predict daily TMAX anomalies ($0.38 \leq R^2 \leq 0.80$) as opposed to
 419 absolute values, and the TMAX seasonal cycle ($0.92 \leq R^2 \leq 0.99$, $0.58^\circ\text{C} \leq \text{RMSE} \leq 1.16^\circ\text{C}$);
 420 Figures S1 and S2.)

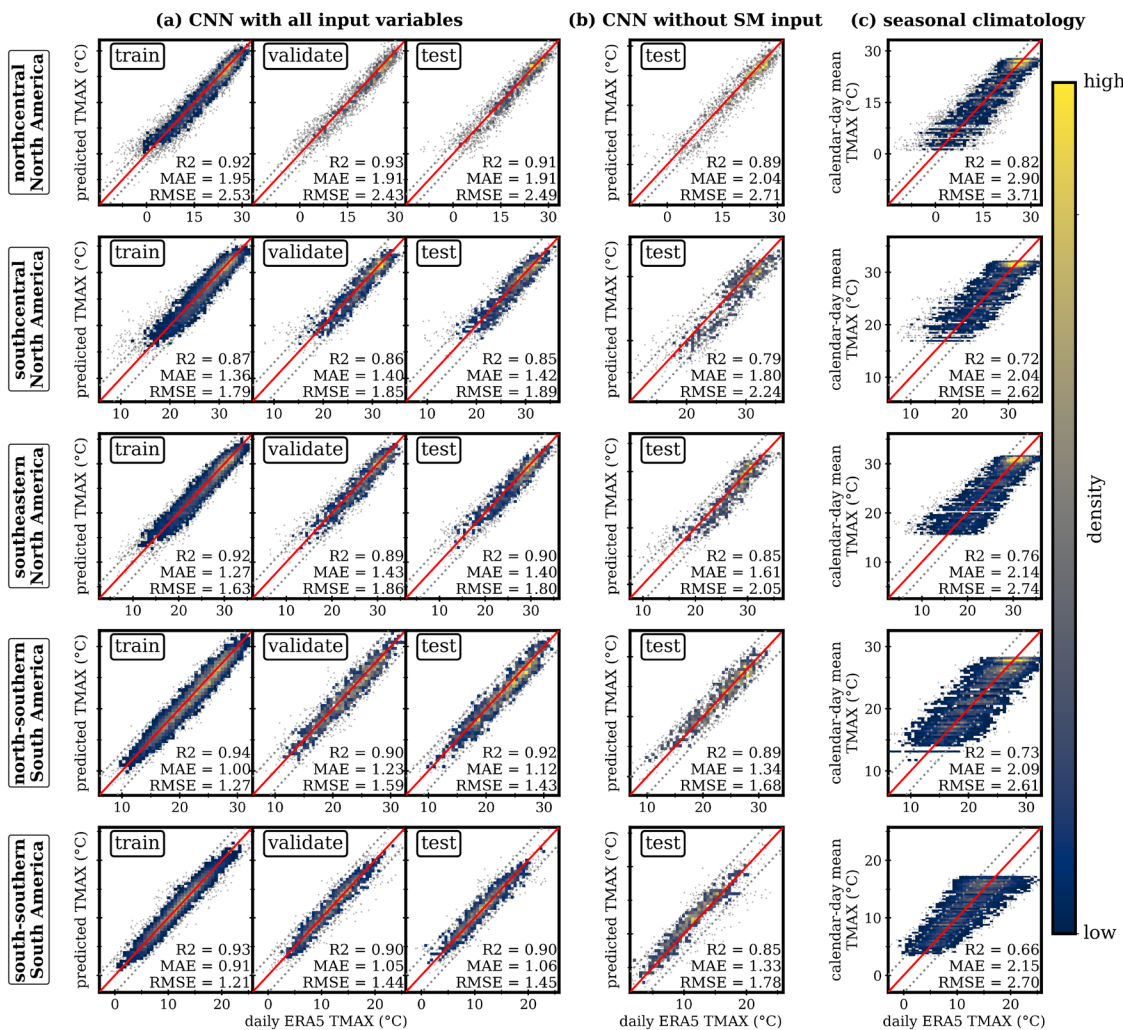


Figure 4. CNN model skill comparison for North and South American regions. (a) Comparison between ERA5-Land TMAX and predicted TMAX from convolutional neural networks (CNNs) trained with daily geopotential height anomaly maps, soil moisture anomaly maps (SM), and normalized calendar day inputs. Model performance is shown separately for the 27-year training subset (used to fit CNN weights), the 8-year validation subset (used to optimize hyperparameters), and the 8-year testing subset (unseen data left out of the training process). See Methods for more details on the training, validation, and testing subsets. (b) Same as (a) but for CNNs trained without the SM inputs. Model performance is shown for the 8-year testing subset. (c) The seasonal climatology of TMAX as shown by comparing the ERA5-Land daily TMAX and the calendar-day mean TMAX each day (averaged over 1979-2021). Each subplot shows the coefficient of determination (R^2), mean absolute error (MAE), and mean squared error (MSE). Correct predictions fall along the 1-1 line (red). Gray dotted lines show ± 3 degrees C prediction errors.

421
 422 We also find large differences in model performance between regions (Figures 4-6).
 423 These differences are most obvious between seasonal-climatology baselines, where RMSE
 424 ranges from $2.40^\circ\text{C} - 3.86^\circ\text{C}$ (southeastern Asia-northeastern Europe) and R^2 ranges from 0.34-
 425 0.88 (southeastern Africa-northeastern Asia; Figures 4-6(a)). These regional differences in model
 426 performance can be explained by the statistics of the underlying TMAX target data. In general,

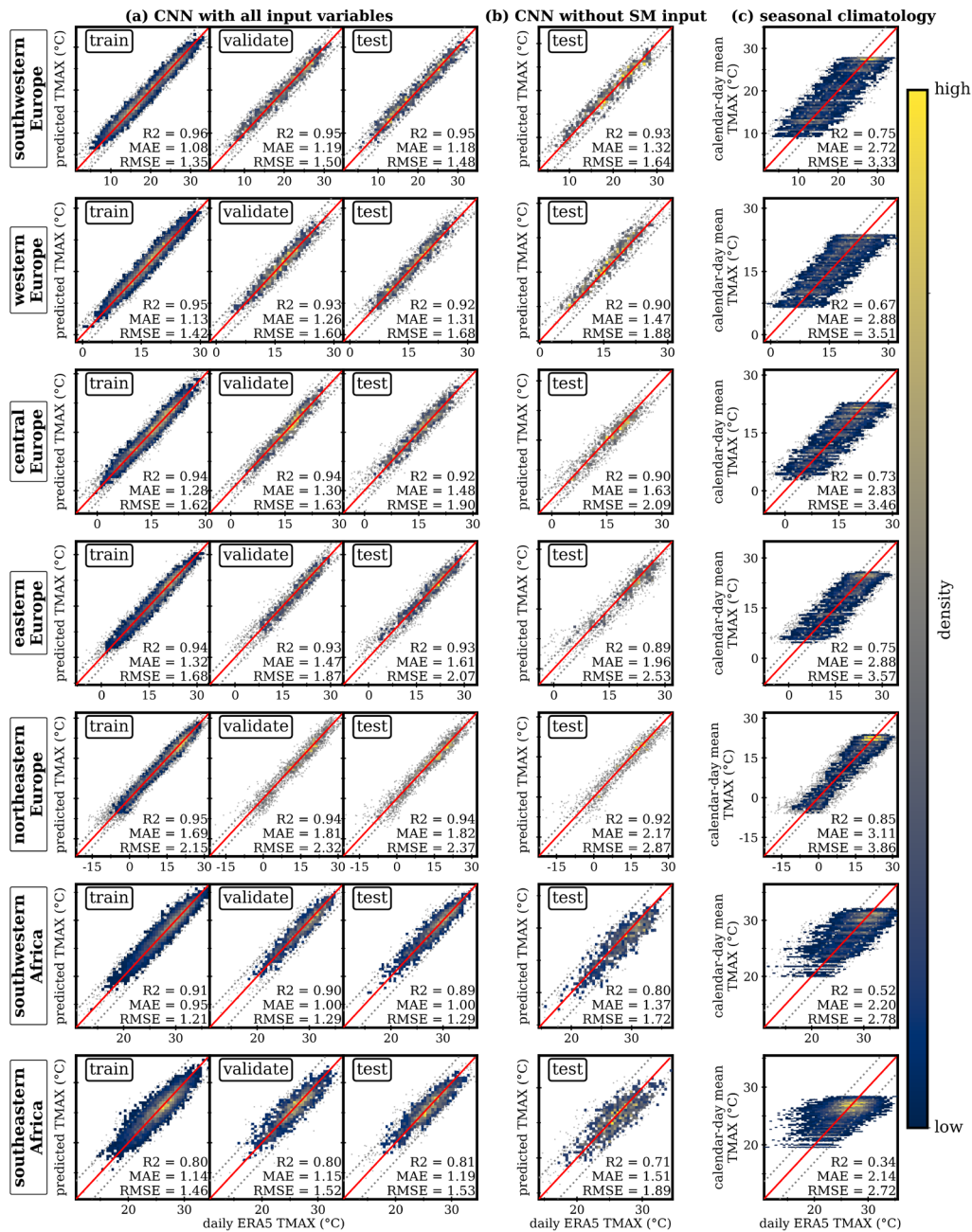
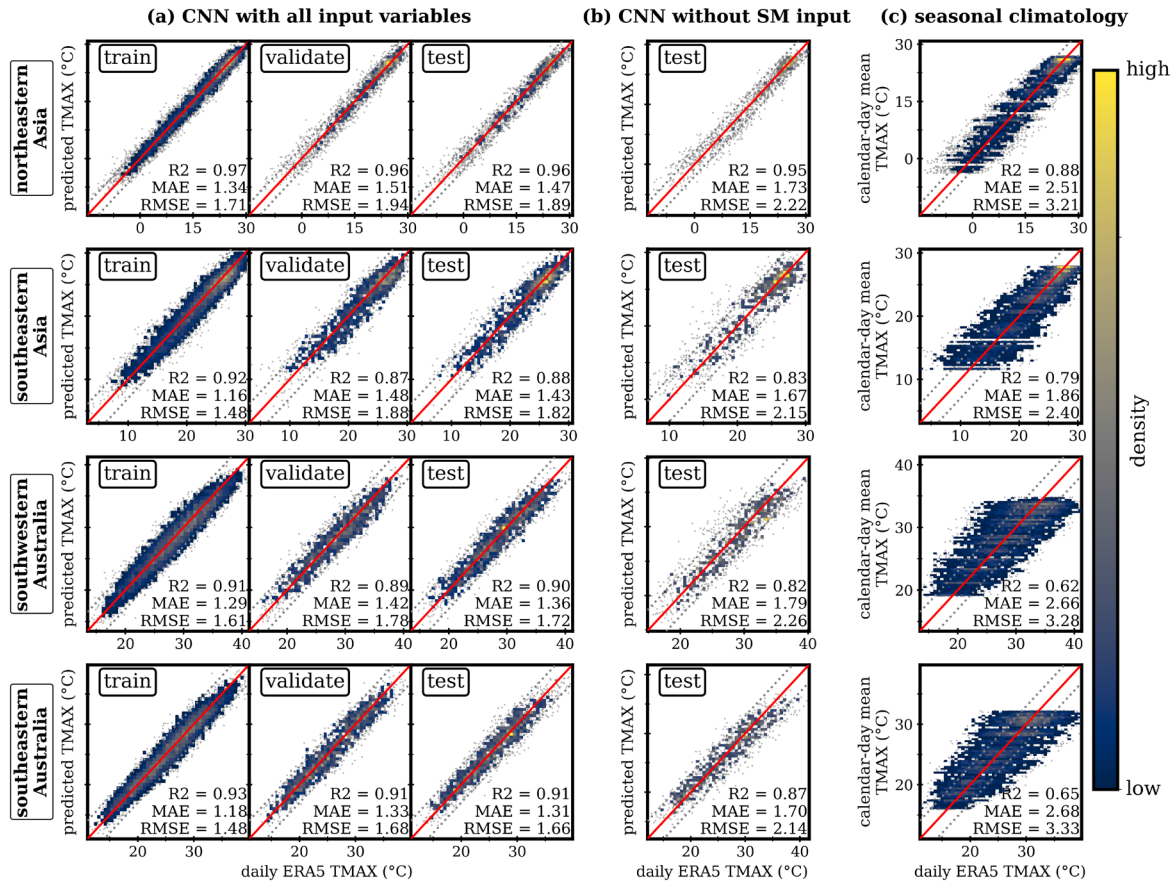


Figure 5. Same as Figure 4, but for regions in Europe and Africa.

427

428 the skill metrics (R^2 , MAE, and RMSE) of the seasonal-climatology baseline are determined by
 429 the magnitude of the region's seasonal cycle and the standard deviation of the daily anomalies
 430 about the seasonal cycle. For example, regions with strong TMAX seasonal cycles (northcentral
 431 North America, northeastern Europe, and northeastern Asia; Figure 3) exhibit higher R^2 values
 432 relative to regions with weak TMAX seasonal cycles (southeastern Africa and southwestern
 433 Africa). Meanwhile, regions with low TMAX standard deviations about the seasonal cycle
 434 (southeastern Asia, north-southern South America, southeastern Africa, and southcentral North

435 America; Figure 3) tend to have lower RMSE than regions with high TMAX standard deviations
 436 about the seasonal cycle (northeastern Europe, northcentral North America, central Europe, and
 437 eastern Europe).



438 **Figure 6.** Same as Figure 4, but for regions in Eastern Asia and Australia.

439

440

3.2 Using Partial Dependence to Investigate SM-T Coupling

441 After evaluating the performance of each regional CNN (Figure 4-6), we apply the partial
 442 dependence analysis method (Figure 2) to obtain the ERA5 summertime SM-T relationships for
 443 each region (Figure 7). The resulting nonlinear SM-T partial dependence plots (PDPs) quantify
 444 how the CNN's average TMAX prediction depends on the average SM input, with areas of
 445 nonzero PDP slope indicating that the prediction is sensitive to the local SM anomaly calculated
 446 from the SM input map. Across all sixteen regions, we find that the SM-T PDPs are negatively
 447 sloped across the entire SM domain (aside from a positive slope in northcentral North America
 448 for wet SM anomalies; Figure 7). This pattern indicates that the CNNs tend to predict higher
 449 TMAX values when SM conditions are drier, and lower TMAX values when SM conditions are
 450 wetter.

451 Despite these overall similarities in the PDP shapes, there are also distinct regional
 452 differences in the ERA5 SM-T relationship (Figure 7). For some regions (e.g., eastern Europe,
 453 southeastern North America), we find that the slope of the SM-T relationship is relatively

454 constant across the entire range of SM anomalies. Other regions exhibit nonlinear SM-T
 455 relationships indicating that the CNN has learned a different relationship between the SM input
 456 map and the TMAX output under different magnitudes of SM anomaly. In many regions, this
 457 nonlinear behavior is observed over a large portion of the SM range (e.g., southwestern
 458 Australia, northcentral North America), while other regions experience nonlinear SM-T behavior
 459 only during the most extreme SM conditions (e.g., the relatively flat PDP slope in southeastern
 460 Australia during extreme wet conditions). To assess the uncertainty associated with each regional
 461 SM-T relationship, we visualize the distribution of local SM anomalies in the training dataset to
 462 identify particular ranges of SM conditions where SM-T relationships may have higher
 463 uncertainty due to underrepresentation in the training dataset (Figure 7). Additionally, we find
 464 that the 5th-95th percentile ranges are narrowest near the origin (SM=0) and become wider near
 465 the tails of the SM distribution indicating that the SM-T relationships are more uncertain during
 466 extreme SM conditions where there are fewer testing samples available.

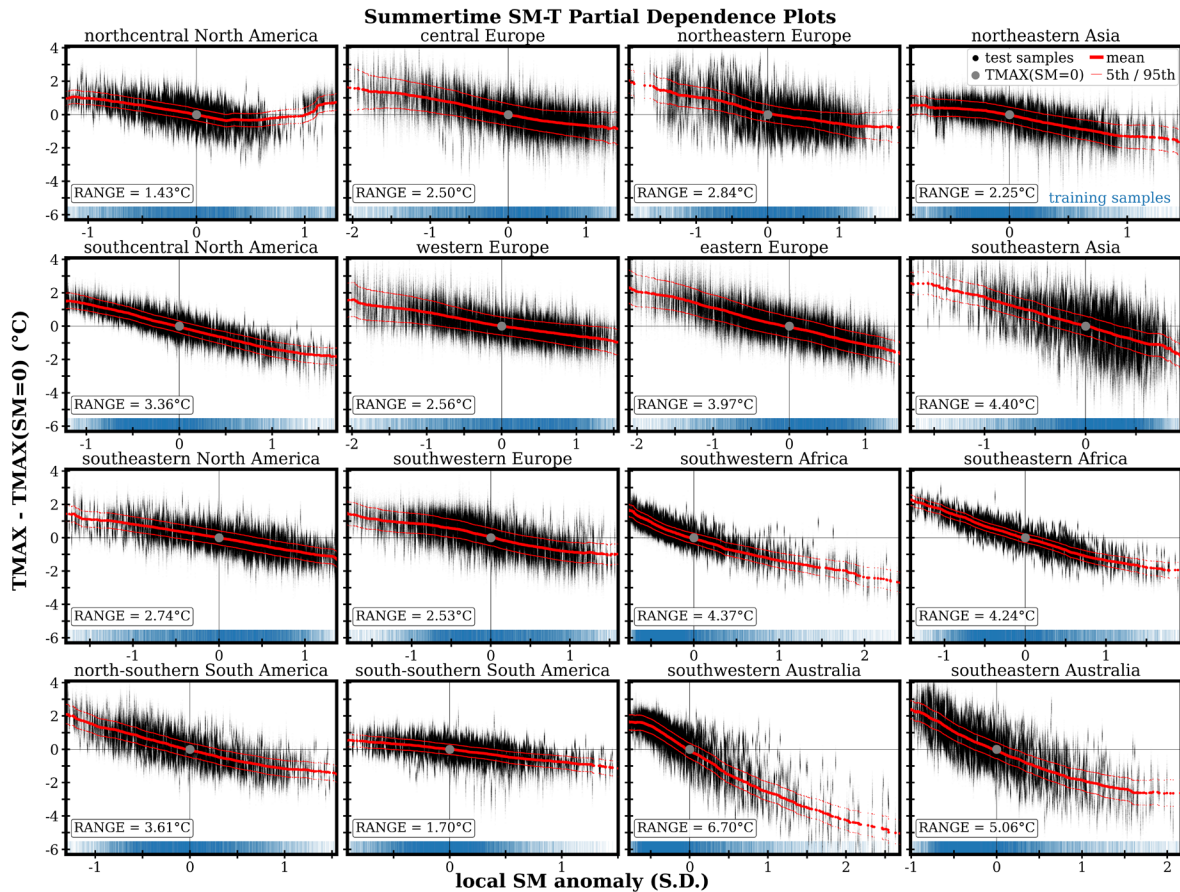


Figure 7. Soil moisture-temperature (SM-T) relationships obtained through partial dependence analysis of convolutional neural networks (method detailed in Figure 2). The smoothed moving average (thick red line) shows the average behavior of the neural network's prediction as the SM input varies from dry (negative) to wet (positive) anomalies. Also shown are the moving 5th and 95th percentiles of the temperature predictions (thin red lines). The SM-T relationships shown are calculated from the testing dataset. We also include a rug plot showing the distribution of SM anomalies in the training dataset. For each subplot, we calculate the range (vertical extent) of the mean SM-T relationship. Soil moisture anomalies are calculated as standard deviations (S.D.) from the calendar-day mean.

467

468 The vertical extent (range) of these SM-T relationships can be used as a relative measure
 469 of regional SM-T coupling strength by estimating the overall potential for SM to influence the

470 CNN’s TMAX prediction on a typical summer day. In North America, we find that southcentral
 471 North America has an SM-T coupling strength of approximately 3.4°C, much higher than both
 472 northcentral North America (1.4°C) and southeastern North America (2.7°C). In Europe, we find
 473 the strongest coupling in eastern Europe (4.0°C) and northeastern Europe (2.8°C), and weaker
 474 coupling in central Europe (2.5°C) and western Europe (2.6°C), and southwestern Europe
 475 (2.5°C). Additionally, we find that southeastern Asia (4.4°C) has stronger coupling than
 476 northeastern Asia (2.3°C), and north-southern South America (3.6°C) has stronger coupling than
 477 south-southern South America (1.7°C), whereas southeastern Africa (4.2°C) and southwestern
 478 Africa (4.4°C) have approximately equal coupling. Finally, southeastern Australia (5.1°C) and
 479 southwestern Australia (6.7°C) have the strongest overall coupling. (We also show sub-regional
 480 variations in SM-T coupling for southcentral North America; Figure S3.)

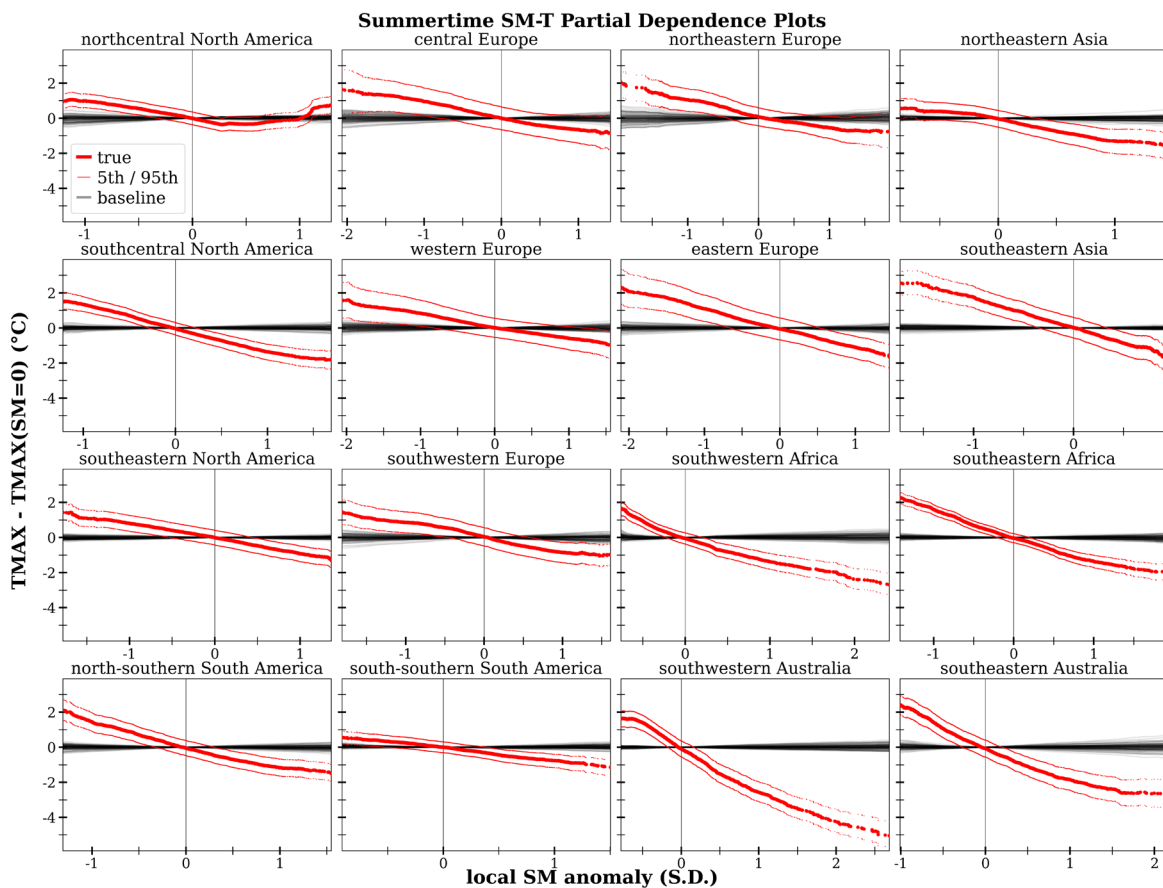


Figure 8. Regional soil moisture-temperature (SM-T) relationships obtained through partial dependence analysis (method detailed in Figure 2) of convolutional neural networks (CNNs) trained to predict regional daily maximum temperature (TMAX) given geopotential height, calendar-day, and soil moisture inputs. Each regional subplot shows 101 SM-T partial dependence plots (PDPs), consisting of the true SM-T PDP (red; Figure 7) and 100 baseline SM-T PDPs (black) derived from CNNs trained with shuffled soil moisture inputs (each shuffled using a different random seed). Also shown are the moving 5th and 95th percentiles of the true SM-T PDP (thin red lines). Soil moisture anomalies are calculated as standard deviations (S.D.) from the calendar-day mean.

481

482 To determine whether each PDP exhibits an SM-T relationship beyond that of random
 483 noise, we compare the true ERA5 SM-T PDPs (Figure 7) against 100 baseline PDPs calculated
 484 from 100 different CNNs trained with randomly shuffled SM input maps—each with a different
 485 random seed (Figure 8). (For illustration, we show a separate example of one of these baseline
 486 PDPs along with a density plot of TMAX predictions in Figure S4.) Across the regions, all 100

487 baseline SM-T PDPs have approximately zero slope over the entire SM domain, with no single
 488 baseline PDP exhibiting a coupling strength greater than 1.2°C (northeastern Europe). We also
 489 find that the vast majority of points along the true regional SM-T PDPs lie far outside the range
 490 of the baselines. Wet SM anomalies (0.5-1.0 standard deviations) in northcentral North America
 491 are the only notable exceptions for which a substantial portion of the regional PDP falls within
 492 the range of the baselines (Figure 8).

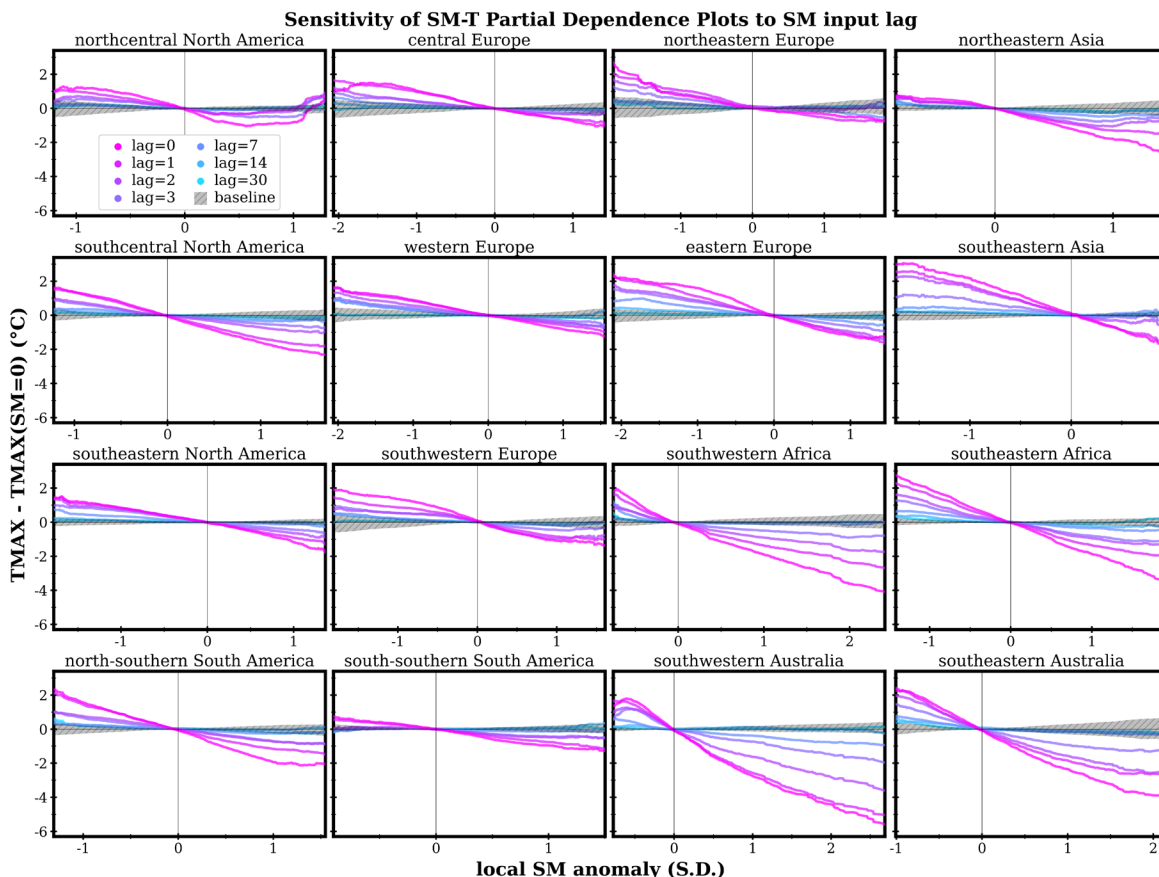


Figure 9. Regional soil moisture-temperature (SM-T) partial dependence relationships obtained using the method detailed in Figure 2 (but for CNNs trained with various levels of soil moisture input lag). Each regional subplot shows SM-T relationships derived from 7 different CNNs trained to predict daily TMAX given the following inputs: calendar day, daily GPH anomaly map, and a single day's SM anomaly map lagged by 0-30 days prior to the prediction day. After the training process, CNN weights are saved and used to calculate the SM-T PDPs as in Figure 2. Colors show SM-T relationships for CNNs trained with SM input lags of 0, 1, 2, 3, 7, 14, and 30 days. Hatching shows the range of 100 baseline PDPs trained with shuffled SM maps (Figure 8). Soil moisture anomalies are calculated as standard deviations (S.D.) from the calendar-day mean.

493

494 We also analyze the sensitivity of regional SM-T relationships to the choice of SM input
 495 lag (Figure 9). Specifically, we show SM-T PDPs derived from seven different CNNs each
 496 trained with different levels of SM input lag. (For example, lag = 3 implies that the CNN is
 497 trained to predict TMAX using the calendar day and GPH input from the prediction day, and the
 498 SM anomaly map from 3 days prior to the prediction day.) In general, although the PDP shape is
 499 similar across input lags, almost all regions experience a monotonic attenuation of SM-T
 500 coupling strength (amplitude) as SM input lag increases from 0 to 30 days. This attenuation is
 501 expected, based on the autocorrelation timescales of top-layer SM. However, the rate of
 502 attenuation varies between the regions. For example, over many regions (south-southern South
 503 America, northcentral North America, northeastern Europe), this attenuation is quite strong and

504 SM-T relationships fall within the range of baseline PDPs for SM lags greater than 3 days. For
505 other regions, this attenuation is much weaker, and we find SM-T coupling relationships that fall
506 outside the range of baseline PDPs at 7-day SM lags (central Europe, northeastern Asia,
507 southwestern Africa), and 14-day SM lags (southcentral North America, southeastern North
508 America, eastern Europe, western Europe, southwestern Europe, southeastern Asia, southeastern
509 Africa, north-southern South America, southwestern Australia, southeastern Australia). Indeed,
510 for extremely dry SM anomalies, some regions exhibit SM-T relationships beyond random noise
511 for SM lags up to 30 days (southwestern Australia, southeastern Australia, southeastern Africa,
512 north-southern South America).

513 We repeat our analysis for all sixteen regions using the NCEP/DOE Reanalysis II dataset
514 over the same time period (1979-2021) at the same $1.875^\circ \times 1.875^\circ$ horizontal resolution (Figures
515 S5-S11). Despite some notable differences in northcentral North America, the resulting NCEP
516 SM-T relationships are consistent with the ERA5 analysis for regional PDP shape (Figure 7 vs.
517 S9), SM-T coupling strengths, comparison with baseline PDPs (Figure 8 vs. S10), and the
518 attenuation of coupling strength with input lag (Figure 9 vs. S11).

519

520 **4 Discussion**

521 We use CNNs (Figure 1) to predict daily average TMAX over 16 mid-latitude regions,
522 and apply partial dependence analysis (Friedman, 2001; Figure 2) to investigate regional SM-T
523 coupling relationships using the ERA5 and NCEP reanalysis datasets. Prior to conducting the
524 partial dependence analysis, we first determine whether the CNN is sufficiently accurate to
525 represent SM-T coupling at daily timescales. This is especially important since CNN model skill
526 metrics vary widely between regions (Figures 4-6). As described in the Methods, our two criteria
527 are that the CNN predicts daily TMAX anomalies from the seasonal cycle, and that the SM input
528 contributes to overall CNN performance at daily timescales. After careful model evaluation, we
529 find that all regional CNNs satisfy these criteria (Figures 4-6).

530 We also find that overall model performance is closely tied to the statistics of the
531 underlying TMAX target data. For instance, a simple model which predicts the calendar-day
532 mean TMAX each day has high R^2 and low MSE when asked to predict over a region
533 characterized by a strong TMAX seasonal cycle with low variance about the seasonal cycle (e.g.,
534 southeastern Asia seasonal-climatology baseline model; Figure 6). Despite good performance
535 metrics, this same model is not suitable for partial dependence analysis of daily-scale SM-T
536 coupling because it fails to predict daily TMAX anomalies from the seasonal cycle. As a result,
537 we stress the importance of thoroughly evaluating the CNN model skill (as suggested in Section
538 2.3) to assess performance at various timescales (Figures S1 and S2). Furthermore, we suggest
539 the use of multiple CNNs with different input combinations to verify that each input variable
540 contributes to overall model performance at the desired timescale (Figures 4-6). The results of
541 these verification tests provide confidence in using the regional CNNs to quantify daily-scale
542 SM-T coupling using partial dependence analysis (Figure 2).

543 Our SM-T PDPs show that the CNN TMAX predictions are sensitive to the local SM
544 anomaly over the prediction region (Figure 7 and S9). Additionally, the SM-T PDPs are
545 negatively sloped and roughly monotonic (aside from wet SM anomalies in northcentral North
546 America), with each CNN predicting warmer temperatures associated with dry SM anomalies
547 and cooler temperatures associated with wet SM anomalies. The general shapes of these SM-T

548 PDPs (Figure 7 and S9) are consistent with the well-understood land-atmosphere interactions
549 through which SM conditions modulate the local surface energy budget and influence near-
550 surface temperatures (Alfaro et al., 2006; Dirmeyer, 2011; J. Liu & Pu, 2019; Seneviratne et al.,
551 2010). Previous studies rely on linear statistical methods (such as the correlation between
552 evapotranspiration and temperature) to assess regional differences in land-atmosphere coupling
553 strength (Dirmeyer, 2011; Jaeger et al., 2009; Koster et al., 2004, 2006a, 2009; Miralles et al.,
554 2012; Seneviratne, Lüthi, et al., 2006; Teuling et al., 2009). While these linear methods are well-
555 suited for quantifying regional differences in coupling strength, evidence from climate models
556 and observations suggest that the actual influence of SM on temperature is nonlinear (Benson &
557 Dirmeyer, 2021; Fischer et al., 2007; Jaeger & Seneviratne, 2011; Schwingshackl et al., 2017;
558 Seneviratne et al., 2010).

559 To allow for the potential of these nonlinear SM-T relationships, our method uses CNN
560 machine learning models to quantify the sensitivity of TMAX to SM across a range of different
561 SM values. We find that the SM-T relationships derived from partial dependence analysis
562 (Figure 2) are approximately linear for some regions (e.g., eastern Europe, southeastern North
563 America) and nonlinear for other regions (e.g., southwestern Australia, northcentral North
564 America, southeastern Australia) (Figure 7). These results suggest that the land-atmosphere
565 interactions that couple daily SM conditions and near-surface TMAX vary under different ranges
566 of SM anomaly, but these variations are regionally dependent. When evaluating these SM-T
567 relationships, it is important to consider that the PDP behavior is most uncertain at the tails of the
568 SM distribution where the 5th-95th percentile ranges are widest and where the
569 underrepresentation of extreme SM anomalies in the training dataset limits the CNNs ability to
570 learn the relationship between SM and TMAX.

571 In order to compare our results more directly with previous assessments of SM-T
572 coupling, we use the vertical extent (range) of our SM-T PDPs (Figure 7) as a relative indicator
573 of SM-T coupling strength. Using this metric, we find much stronger JJA SM-T coupling in
574 southcentral North America compared to northcentral North America and southeastern North
575 America. This agrees with previous assessments of land-atmosphere coupling strength using
576 climate models (Koster et al., 2006a, 2009; Seneviratne, Lüthi, et al., 2006) and observational
577 datasets (Dirmeyer, 2011; Miralles et al., 2012). These results are also consistent with Teuling et
578 al., (2009) and Schwingshackl et al., (2017), who used observational and reanalysis datasets,
579 respectively, to classify southcentral North America and northcentral North America as regions
580 with a high potential for strong SM-T coupling and southeastern North America as a region with
581 little potential for SM-T coupling.

582 In Europe, we find that our northeastern Europe and eastern Europe regions have the
583 strongest PDP-based SM-T coupling strength, while our central Europe, western Europe, and
584 southwestern Europe regions have the weakest (Figure 7). This hierarchy of coupling strength in
585 Europe is consistent with Fischer et al., (2007), whose regional climate model experiments
586 identified the strongest 2003 JJA SM-T coupling in eastern Europe (followed by central Europe
587 and western Europe), and the weakest coupling in southwestern Europe (with northeastern
588 Europe not considered in their domain). Seneviratne, Lüthi, et al., (2006) and Jaeger et al.,
589 (2009) also found strong JJA SM-T coupling in eastern Europe and northeastern Europe, with
590 weaker coupling in western Europe and central Europe. Our results are also consistent with
591 Teuling et al., (2009) who found the potential for strong SM-T coupling in eastern Europe and
592 northeastern Europe. However, numerous previous studies (Dirmeyer, 2011; Jaeger et al., 2009;

593 Miralles et al., 2012; Seneviratne, Lüthi, et al., 2006; Teuling et al., 2009) all identified strong
594 SM-T coupling over southwestern Europe, in contrast to our PDP-based results (although
595 Seneviratne, Lüthi, et al., 2006, warn that certain coupling metrics, like the correlation of
596 evapotranspiration and 2-meter temperature, may not be meaningful in regions with small
597 evapotranspiration like southwestern Europe).

598 In the Southern Hemisphere, our PDP-based SM-T coupling strengths show weak
599 coupling in south-southern South America, and strong coupling in north-southern South
600 America, southwestern Africa, southeastern Africa, southwestern Australia, and southeastern
601 Australia (Figure 7). These PDP-based coupling strengths are remarkably consistent with
602 Dirmeyer, (2011), who analyzed coupling between latent heat flux and SM to identify regions
603 with strong SM-T coupling potential. Our results are also consistent with Schwingshackl et al.,
604 (2017), who identified south-southern South America as a wet SM regime during DJF, and all
605 other regions (north-southern South America, southwestern Africa, southeastern Africa,
606 southwestern Australia, and southeastern Australia) as transitional SM regimes. In South
607 America, Miralles et al., (2012) found approximately equal coupling across central and south-
608 southern South America, although numerous other studies (e.g., Baker et al., 2021; Dirmeyer,
609 2011; Menendez et al., 2019; Ruscica et al., 2014; Spennemann et al., 2018) report that land-
610 atmosphere coupling is much stronger in north-southern South America compared to south-
611 southern South America. The results of Miralles et al., (2012) also support our conclusion that
612 SM-T coupling is much stronger in Africa and Australia compared to South America.

613 The most notable differences between our results and previous assessments of regional
614 SM-T coupling strengths occur in eastern Asia. Using both the ERA5 and NCEP datasets, we
615 find substantially stronger PDP-based SM-T coupling in our southeastern Asia region compared
616 to our northeastern Asia region (Figures 7 and S9, respectively). Previous studies report roughly
617 equal (Koster et al., 2006a) or substantially stronger coupling in northeastern Asia (Dirmeyer,
618 2011; Koster et al., 2009; Miralles et al., 2012; Schwingshackl et al., 2017; Seneviratne, Lüthi, et
619 al., 2006; Teuling et al., 2009), which conflicts with our ERA5 and NCEP results.

620 We extend our partial dependence analysis to modified versions of our training dataset,
621 which yields additional insights into the timescale of SM memory within the SM-T relationship.
622 We find a monotonic attenuation of PDP-based coupling strength with increasing SM input lag
623 (Figure 9). The overall reduction in SM-T coupling strength is likely a consequence of limited
624 SM memory as the SM input becomes less physically relevant to actual conditions on the
625 prediction day. Our results also agree with previous studies which suggest that wet SM
626 anomalies decay faster than dry SM anomalies (Orth & Seneviratne, 2012; Song et al., 2019),
627 resulting in longer SM memory for extreme dry conditions (Orth & Seneviratne, 2012).
628 Specifically, we find that in 12 of the 16 regions, the SM-T relationship remains outside the
629 range of random noise at longer lags for dry anomalies than for wet anomalies (Figure 9). In
630 addition, we find regional differences in the timescale of decay in PDP-based coupling strength
631 as SM input lag increases (Figure 9). For example, southeastern Africa (among other regions)
632 exhibits an SM-T relationship beyond random noise at lags up to 14 days. However, SM-T
633 relationships in south-southern South America, northcentral North America, and northeastern
634 Europe fall within the range of random noise beyond 3-day SM lags. These regional differences
635 in PDP attenuation agree reasonably well with Seneviratne, Koster, et al., (2006), who found
636 long SM memories across southern Africa, Australia, Europe, North America, and north-
637 southern South America, but substantially shorter SM memory in northeastern Asia and south-

638 southern South America. Seneviratne, Koster, et al., (2006) also found long SM memory in
639 southeastern Asia which conflicts with our ERA5 and NCEP results. Overall, these results
640 suggest that incorporating additional temporal SM information from 7-, 14-, or even 30-days
641 prior to the TMAX prediction could improve the CNN's ability to predict TMAX.

642 Our analysis focuses specifically on SM-T coupling over midlatitude regions; however,
643 the physical processes that regulate SM-T interactions may be different in tropical and high-
644 latitude regions. Therefore, though the flexibility of our machine learning-based framework
645 makes it deployable to other regions, we do not claim that our results can be applied to other
646 areas of the globe (such as in the tropics or high latitudes) without further investigation. We also
647 acknowledge that there may exist different configurations of machine learning model (e.g., long
648 short-term memory network), hyperparameters, and input variables that are able to achieve better
649 performance than the CNNs used in this study. Regardless, our results show that these CNNs
650 capture SM-T relationships that broadly agree with previous assessments of SM-T coupling. We
651 also recognize that our regional assessment of SM-T coupling fails to capture fine-scale spatial
652 differences in coupling found in previous studies (e.g., Koster et al., 2006b; Miralles et al.,
653 2012). However, our framework could be readily extended to assess coupling at finer spatial
654 resolutions by calculating SM-T relationships over smaller subregions (Figure S3) and/or using
655 input data with finer spatial resolution. Though we focus specifically on the relationship between
656 surface-layer SM and TMAX (which is most relevant for daily-scale SM-T coupling), our
657 analysis could also be modified to assess coupling between numerous other land-surface and
658 atmospheric variables (e.g., coupling between latent heat flux and daily mean temperature,
659 coupling between evapotranspiration and precipitation).

660 Although our PDPs quantify the average impact of local SM conditions on the CNN's
661 TMAX prediction, there may be other processes correlated with SM conditions whose effect on
662 temperature is incorrectly attributed to SM. One way to address this would be to repeat this
663 analysis using a different land-surface variable in place of SM (e.g., latent heat flux or
664 evapotranspiration) and compare the corresponding coupling relationships with temperature.
665 Another approach would be to include additional atmospheric and land-surface variables as CNN
666 inputs and hold them constant during the PDP calculation to isolate the effect of SM alone on
667 temperature. However, adding additional variables would run the risk of violating the
668 independence assumption between input variables. Indeed, although we use standardized
669 calendar-day anomalies for SM and GPH inputs to avoid seasonal dependencies with the
670 calendar-day inputs, a side effect is that our PDPs are calculated in terms of standardized SM
671 anomalies instead of the raw SM fraction values. Since each SM grid cell's calendar-day mean
672 and standard deviation fluctuates throughout the summer, we cannot convert SM anomalies
673 directly back to SM fraction values, which prevents us from being able to compare the
674 magnitude of the PDP slope directly between regions.

675 Finally, like all SM-T coupling assessments, our results are also dataset-dependent.
676 Although it represents an improvement over the land component of previous reanalyses, the
677 ERA5-Land surface-layer soil moisture dataset used in this analysis has a known wet-bias and
678 exhibits regional differences in agreement (i.e., correlation) when compared to 5-cm in situ
679 observations of SM across Europe, North America, and Australia (Muñoz-Sabater et al. 2021).
680 As a result, the SM-T relationships presented here may be more representative of the real world
681 in regions where the ERA5-Land SM closely matches observations, and less representative in
682 regions where the ERA5-Land SM has higher uncertainty. Regardless, while the results

683 presented here are limited to the datasets that were analyzed, our framework could easily be
684 extended to quantify SM-T relationships using a wide range of datasets from climate models,
685 reanalyses, remote sensing, and/or gridded observations.

686

687 **5 Conclusions**

688 We present a new approach for quantifying soil moisture-temperature (SM-T) coupling
689 which uses convolutional neural network (CNN) machine learning models and partial
690 dependence plots (PDPs) to visualize nonlinear SM-T relationships over 16 mid-latitude regions
691 in the Northern and Southern Hemispheres. From these regional SM-T relationships, we find that
692 the CNNs predict warmer temperatures when the soils are dry and cooler temperatures when the
693 soils are wet, which is consistent with well-understood land-atmosphere interactions in the mid-
694 latitudes. We also find that our relative measure of SM-T coupling strength broadly agrees with
695 previous assessments of regional SM-T coupling. Though our approach is designed to allow for
696 the potential of nonlinear SM-T relationships, we find that the SM-T PDPs are approximately
697 linear over several regions, such as eastern Europe and southeastern North America. That said,
698 other regions exhibit pronounced nonlinear behavior across a large portion of the SM range (e.g.,
699 southwestern Australia, northcentral North America). This nonlinearity suggests that the coupled
700 interactions governing the SM-T relationship vary under different SM conditions, but these
701 variations are regionally dependent. Taken together, our results show that PDPs can be combined
702 with CNNs to create a powerful tool for quantifying nonlinear SM-T coupling relationships.

703 In particular, we find that applying machine-learning interpretation and visualization
704 techniques (i.e., PDPs) to modified versions of our training datasets can yield new insights into
705 physical processes, such as the nonlinear characteristics of SM memory, which is a vital
706 component of long-term SM-T coupling. For example, in accordance with previous studies, we
707 find that SM memory fades monotonically over time, and that wet SM anomalies fade faster than
708 dry anomalies. More research is required to understand the full potential for PDPs to reveal
709 regional differences in the nonlinear properties of SM memory, with implications for seasonal
710 forecasting of temperature and precipitation.

711 Partial dependence analysis has only recently been applied to CNNs for geoscience
712 applications. However, we suggest that many complex climate processes have the potential to be
713 studied by analyzing CNNs with PDPs as long as enough high-quality training data are available.
714 For example, given sufficient training data, our analysis could be extended to investigate
715 climate-driven changes in SM-temperature and SM-precipitation coupling at daily and seasonal
716 timescales using climate model simulations under historic and future climate change scenarios.
717 Likewise, PDPs with CNNs could be used to explore non-local coupling relationships between
718 land, ocean, and atmospheric conditions which can improve our understanding of complex
719 climate processes such as the El Niño Southern Oscillation. More generally, our results show that
720 PDPs can be an effective tool for quantifying nonlinear coupling relationships between the
721 CNN's output prediction and quantities calculated from the input maps. We emphasize that, for
722 each of these potential applications, even if the training data appears to be adequate, each CNN
723 model must be thoroughly evaluated to ensure that the model is trustworthy and is representative
724 of physical processes in the real world.

725 Coupled interactions in the Earth system are important drivers of climate variability and
726 extreme weather events, but many of these coupled processes are still not fully understood.

727 Based on our results, partial dependence analysis is a promising pathway for using CNNs to
728 investigate these nonlinear coupled interactions, with important implications for model
729 development, model parameterization, and seasonal forecasting.

730

731 **Open Research**

732

733 The hourly ERA5 (Hersbach, H., et al., 2018) and ERA5-Land (Muñoz Sabater, J., 2021)
734 data are available from the Copernicus Climate Change Service Climate Data Store and can be
735 accessed from their website at [https://cds.climate.copernicus.eu/cdsapp#!/dataset/reanalysis-
736 era5-pressure-levels](https://cds.climate.copernicus.eu/cdsapp#!/dataset/reanalysis-era5-pressure-levels) and <https://cds.climate.copernicus.eu/cdsapp#!/dataset/reanalysis-era5-land>,
737 respectively. The daily mean NCEP/DOE Reanalysis II data (Kanamitsu et al. 2002) provided by
738 the NOAA PSL, Boulder, Colorado, USA, is available from their website at
739 <https://psl.noaa.gov/data/gridded/data.ncep.reanalysis2.html>. Analysis code will be available on
740 Zenodo via DOI (set at time of publication).

741

742 **Acknowledgments**

743

744 We thank three anonymous reviewers for insightful and constructive comments.
745 Computational resources were provided by the Stanford Research Computing Center and
746 Stanford’s Center for Computational Earth and Environmental Sciences. This work was
747 supported by Stanford University and NSF CAREER grant AGS-1749261.

748

749 **References**

750

- 751 Alfaro, E. J., Gershunov, A., & Cayan, D. (2006). Prediction of Summer Maximum and
752 Minimum Temperature over the Central and Western United States: The Roles of Soil
753 Moisture and Sea Surface Temperature. *Journal of Climate*, 19(8), 1407–1421.
754 <https://doi.org/10.1175/JCLI3665.1>
- 755 Bach, S., Binder, A., Montavon, G., Klauschen, F., Müller, K.-R., & Samek, W. (2015). On
756 Pixel-Wise Explanations for Non-Linear Classifier Decisions by Layer-Wise Relevance
757 Propagation. *PloS One*, 10(7), e0130140. <https://doi.org/10.1371/journal.pone.0130140>
- 758 Baker, Jessica C. A., Dayana Castilho de Souza, Paulo Y. Kubota, Wolfgang Buermann, Caio A.
759 S. Coelho, Martin B. Andrews, Manuel Gloor, Luis Garcia-Carreras, Silvio N. Figueroa,
760 and Dominick V. Spracklen. (2021). “An Assessment of Land–Atmosphere Interactions
761 over South America Using Satellites, Reanalysis, and Two Global Climate Models.”
762 *Journal of Hydrometeorology* 22 (4): 905–22.
- 763 Barnes, E. A., Mayer, K. J., Rader, J., Toms, B. A., & Ebert-Uphoff, I. (2020). Leveraging
764 Interpretable Neural Networks for Scientific Discovery. 2020, A069–03.
765 <https://ui.adsabs.harvard.edu/abs/2020AGUFMA069...03B>

- 766 Barnes, E. A., Toms, B., Hurrell, J. W., Ebert-Uphoff, I., Anderson, C., & Anderson, D. (2020).
767 Indicator Patterns of Forced Change Learned by an Artificial Neural Network. *Journal of*
768 *Advances in Modeling Earth Systems*, 12(9), e2020MS002195.
769 <https://doi.org/10.1029/2020MS002195>
- 770 Benson, D. O., & Dirmeyer, P. A. (2021). Characterizing the Relationship between Temperature
771 and Soil Moisture Extremes and Their Role in the Exacerbation of Heat Waves over the
772 Contiguous United States. *Journal of Climate*, 34(6), 2175–2187.
773 <https://doi.org/10.1175/JCLI-D-20-0440.1>
- 774 Bolton, T., & Zanna, L. (2019). Applications of deep learning to ocean data inference and
775 subgrid parameterization. *Journal of Advances in Modeling Earth Systems*, 11(1), 376–
776 399. <https://doi.org/10.1029/2018ms001472>
- 777 Buja, A., Cook, D., Hofmann, H., Lawrence, M., Lee, E.-K., Swayne, D. F., & Wickham, H.
778 (2009). Statistical inference for exploratory data analysis and model diagnostics.
779 *Philosophical Transactions. Series A, Mathematical, Physical, and Engineering Sciences*,
780 367(1906), 4361–4383. <https://doi.org/10.1098/rsta.2009.0120>
- 781 Cattiaux, J., Douville, H., & Peings, Y. (2013). European temperatures in CMIP5: origins of
782 present-day biases and future uncertainties. *Climate Dynamics*, 41(11), 2889–2907.
783 <https://doi.org/10.1007/s00382-013-1731-y>
- 784 Chen, Ajiao, Huade Guan, Okke Batelaan, Xinping Zhang, and Xinguang He. (2019). “Global
785 Soil Moisture-air Temperature Coupling Based on GRACE-derived Terrestrial Water
786 Storage.” *Journal of Geophysical Research* 124 (14): 7786–96.
- 787 Chilson, C., Avery, K., McGovern, A., Bridge, E., Sheldon, D., & Kelly, J. (2019). Automated
788 detection of bird roosts using NEXRAD radar data and Convolutional Neural Networks.
789 *Remote Sensing in Ecology and Conservation*, 5(1), 20–32.
790 <https://doi.org/10.1002/rse2.92>
- 791 Davenport, F. V., & Diffenbaugh, N. S. (2021). Using machine learning to analyze physical
792 causes of climate change: A case study of U.s. midwest extreme precipitation.
793 *Geophysical Research Letters*, 48(15). <https://doi.org/10.1029/2021gl093787>
- 794 Developers, T. (2021). TensorFlow [Software]. <https://doi.org/10.5281/zenodo.5593257>
- 795 Dennis, Eli J., and Ernesto Hugo Berbery. (2021). “The Role of Soil Texture in Local Land
796 Surface–Atmosphere Coupling and Regional Climate.” *Journal of Hydrometeorology* 22
797 (2): 313–30.
- 798 Diffenbaugh, N. S., & Ashfaq, M. (2010). Intensification of hot extremes in the United States.
799 *Geophysical Research Letters*, 37(15). <https://doi.org/10.1029/2010gl043888>
- 800 Diffenbaugh, Noah S., and Elizabeth A. Barnes. (2023). “Data-Driven Predictions of the Time
801 Remaining until Critical Global Warming Thresholds Are Reached.” *Proceedings of the*
802 *National Academy of Sciences of the United States of America* 120 (6): e2207183120.
- 803 Diffenbaugh, N. S., Pal, J. S., Giorgi, F., & Gao, X. (2007). Heat stress intensification in the
804 Mediterranean climate change hotspot. *Geophysical Research Letters*, 34(11).
805 <https://doi.org/10.1029/2007gl030000>
- 806 Dirmeyer, P. A. (2011). The terrestrial segment of soil moisture-climate coupling. *Geophysical*
807 *Research Letters*, 38(16). <https://doi.org/10.1029/2011gl048268>
- 808 Durre, I., Wallace, J. M., & Lettenmaier, D. P. (2000). Dependence of Extreme Daily Maximum
809 Temperatures on Antecedent Soil Moisture in the Contiguous United States during
810 Summer. *Journal of Climate*, 13(14), 2641–2651. [https://doi.org/10.1175/1520-
811 0442\(2000\)013<2641:DOEDMT>2.0.CO;2](https://doi.org/10.1175/1520-0442(2000)013<2641:DOEDMT>2.0.CO;2)

- 812 Dutra, E., Schär, C., Viterbo, P., & Miranda, P. M. A. (2011). Land-atmosphere coupling
 813 associated with snow cover. *Geophysical Research Letters*, 38(15).
 814 <https://doi.org/10.1029/2011gl048435>
- 815 Ebert-Uphoff, I., & Hilburn, K. (2020). Evaluation, Tuning, and Interpretation of Neural
 816 Networks for Working with Images in Meteorological Applications. *Bulletin of the*
 817 *American Meteorological Society*, 101(12), E2149–E2170.
 818 <https://doi.org/10.1175/BAMS-D-20-0097.1>
- 819 Fischer, E. M., Seneviratne, S. I., Vidale, P. L., Lüthi, D., & Schär, C. (2007). Soil Moisture–
 820 Atmosphere Interactions during the 2003 European Summer Heat Wave. *Journal of*
 821 *Climate*, 20(20), 5081–5099. <https://doi.org/10.1175/JCLI4288.1>
- 822 Friedman, J. H. (2001). Greedy Function Approximation: A Gradient Boosting Machine. *Annals*
 823 *of Statistics*, 29(5), 1189–1232. <http://www.jstor.org/stable/2699986>
- 824 Gagne, D. J., II, Haupt, S. E., Nychka, D. W., & Thompson, G. (2019). Interpretable Deep
 825 Learning for Spatial Analysis of Severe Hailstorms. *Monthly Weather Review*, 147(8),
 826 2827–2845. <https://doi.org/10.1175/MWR-D-18-0316.1>
- 827 Gevaert, A. I., D. G. Miralles, R. A. M. de Jeu, J. Schellekens, and A. J. Dolman. (2018). “Soil
 828 Moisture-Temperature Coupling in a Set of Land Surface Models.” *Journal of*
 829 *Geophysical Research* 123 (3): 1481–98.
- 830 Goldstein, A., Kapelner, A., Bleich, J., & Pitkin, E. (2015). Peeking Inside the Black Box:
 831 Visualizing Statistical Learning With Plots of Individual Conditional Expectation.
 832 *Journal of Computational and Graphical Statistics: A Joint Publication of American*
 833 *Statistical Association, Institute of Mathematical Statistics, Interface Foundation of North*
 834 *America*, 24(1), 44–65. <https://doi.org/10.1080/10618600.2014.907095>
- 835 Ham, Y.-G., Kim, J.-H., & Luo, J.-J. (2019). Deep learning for multi-year ENSO forecasts.
 836 *Nature*, 573(7775), 568–572. <https://doi.org/10.1038/s41586-019-1559-7>
- 837 Han, Y., Zhang, G. J., Huang, X., & Wang, Y. (2020). A moist physics parameterization based
 838 on deep learning. *Journal of Advances in Modeling Earth Systems*, 12(9).
 839 <https://doi.org/10.1029/2020ms002076>
- 840 Henderson, G. R., Peings, Y., Furtado, J. C., & Kushner, P. J. (2018). Snow–atmosphere
 841 coupling in the Northern Hemisphere. *Nature Climate Change*, 8(11), 954–963.
 842 <https://doi.org/10.1038/s41558-018-0295-6>
- 843 Hersbach, Bell, & Berrisford. (2018). ERA5 hourly data on pressure levels from 1979 to present.
 844 (c3s) Climate Data [Dataset]
- 845 He, Zhang, Ren, & Sun. (2015). Delving deep into rectifiers: Surpassing human-level
 846 performance on imagenet classification. *Proceedings of the IEEE*.
 847 [http://openaccess.thecvf.com/content_iccv_2015/html/He_Delving_Deep_into_ICCV_20](http://openaccess.thecvf.com/content_iccv_2015/html/He_Delving_Deep_into_ICCV_2015_paper.html)
 848 [15_paper.html](http://openaccess.thecvf.com/content_iccv_2015/html/He_Delving_Deep_into_ICCV_2015_paper.html)
- 849 Hinton, Srivastava, & Swersky. (2012). Neural networks for machine learning lecture 6a
 850 overview of mini-batch gradient descent. Cited on.
 851 <http://www.cs.toronto.edu/~hinton/coursera/lecture6/lec6.pdf>
- 852 Hirsch, A. L., A. J. Pitman, and J. Kala. (2014). “The Role of Land Cover Change in Modulating
 853 the Soil Moisture-Temperature Land-Atmosphere Coupling Strength over Australia.”
 854 *Geophysical Research Letters* 41 (16): 5883–90.
- 855 Horton, D. E., Johnson, N. C., Singh, D., Swain, D. L., Rajaratnam, B., & Diffenbaugh, N. S.
 856 (2015). Contribution of changes in atmospheric circulation patterns to extreme
 857 temperature trends. *Nature*, 522(7557), 465–469. <https://doi.org/10.1038/nature14550>

- 858 Jacques-Dumas, V., Ragone, F., Borgnat, P., Abry, P., & Bouchet, F. (2021). Deep Learning-
859 based Extreme Heatwave Forecast. In arXiv [cs.LG]. arXiv.
860 <http://arxiv.org/abs/2103.09743>
- 861 Jaeger, E. B., & Seneviratne, S. I. (2011). Impact of soil moisture–atmosphere coupling on
862 European climate extremes and trends in a regional climate model. *Climate Dynamics*,
863 36(9), 1919–1939. <https://doi.org/10.1007/s00382-010-0780-8>
- 864 Jaeger, E. B., Stöckli, R., & Seneviratne, S. I. (2009). Analysis of planetary boundary layer
865 fluxes and land-atmosphere coupling in the regional climate model CLM. *Journal of*
866 *Geophysical Research*, 114(D17). <https://doi.org/10.1029/2008jd011658>
- 867 Jergensen, G. E., McGovern, A., Lagerquist, R., & Smith, T. (2019). Classifying convective
868 storms using machine learning. *Weather and Forecasting*, 35(2), 537–559.
869 <https://doi.org/10.1175/waf-d-19-0170.1>
- 870 Kanamitsu, M., Ebisuzaki, W., & Woollen, J. (2002). Ncep–doe amip-ii reanalysis (r-2). *Bulletin*
871 *of the American Meteorological Society*. [Dataset].
872 <https://journals.ametsoc.org/view/journals/bams/83/11/bams-83-11-1631.xml>
- 873 Koster, R. D., Dirmeyer, P. A., Guo, Z., Bonan, G., Chan, E., Cox, P., Gordon, C. T., Kanae, S.,
874 Kowalczyk, E., Lawrence, D., Liu, P., Lu, C.-H., Malyshev, S., McAvaney, B., Mitchell,
875 K., Mocko, D., Oki, T., Oleson, K., Pitman, A., ... GLACE Team. (2004). Regions of
876 strong coupling between soil moisture and precipitation. *Science*, 305(5687), 1138–1140.
877 <https://doi.org/10.1126/science.1100217>
- 878 Koster, R. D., Schubert, S. D., & Suarez, M. J. (2009). Analyzing the Concurrence of
879 Meteorological Droughts and Warm Periods, with Implications for the Determination of
880 Evaporative Regime. *Journal of Climate*, 22(12), 3331–3341.
881 <https://doi.org/10.1175/2008JCLI2718.1>
- 882 Koster, R. D., Sud, Y. C., Guo, Z., Dirmeyer, P. A., Bonan, G., Oleson, K. W., Chan, E.,
883 Verseghy, D., Cox, P., Davies, H., Kowalczyk, E., Gordon, C. T., Kanae, S., Lawrence,
884 D., Liu, P., Mocko, D., Lu, C.-H., Mitchell, K., Malyshev, S., ... Xue, Y. (2006a).
885 GLACE: The Global Land–Atmosphere Coupling Experiment. Part I: Overview. *Journal*
886 *of Hydrometeorology*, 7(4), 590–610. <https://doi.org/10.1175/JHM510.1>
- 887 Koster, R. D., Sud, Y. C., Guo, Z., Dirmeyer, P. A., Bonan, G., Oleson, K. W., Chan, E.,
888 Verseghy, D., Cox, P., Davies, H., Kowalczyk, E., Gordon, C. T., Kanae, S., Lawrence,
889 D., Liu, P., Mocko, D., Lu, C.-H., Mitchell, K., Malyshev, S., ... Xue, Y. (2006b).
890 GLACE: The Global Land–Atmosphere Coupling Experiment. Part I: Overview. *Journal*
891 *of Hydrometeorology*, 7(4), 590–610. <https://doi.org/10.1175/JHM510.1>
- 892 Lagerquist, R., McGovern, A., & Gagne, D. J., II. (2019). Deep Learning for Spatially Explicit
893 Prediction of Synoptic-Scale Fronts. *Weather and Forecasting*, 34(4), 1137–1160.
894 <https://doi.org/10.1175/WAF-D-18-0183.1>
- 895 Larraondo, P. R., Renzullo, L. J., Inza, I., & Lozano, J. A. (2019). A data-driven approach to
896 precipitation parameterizations using convolutional encoder-decoder neural networks. In
897 arXiv [physics.ao-ph]. arXiv. <http://arxiv.org/abs/1903.10274>
- 898 LeCun, Y., Bengio, Y., & Hinton, G. (2015). Deep learning. *Nature*, 521(7553), 436–444.
899 <https://doi.org/10.1038/nature14539>
- 900 LeCun, Y., Boser, B., Denker, J., Henderson, D., Howard, R., Hubbard, W., & Jackel, L. (1989).
901 Handwritten digit recognition with a back-propagation network. *Advances in Neural*
902 *Information Processing Systems*, 2.

- 903 <https://proceedings.neurips.cc/paper/1989/hash/53c3bce66e43be4f209556518c2fcb54->
904 [Abstract.html](https://proceedings.neurips.cc/paper/1989/hash/53c3bce66e43be4f209556518c2fcb54-)
- 905 Liu, J., & Pu, Z. (2019). Does soil moisture have an influence on near-surface temperature?
906 *Journal of Geophysical Research*, 124(12), 6444–6466.
907 <https://doi.org/10.1029/2018jd029750>
- 908 Liu, Y., Racah, E., Prabhat, Correa, J., Khosrowshahi, A., Lavers, D., Kunkel, K., Wehner, M.,
909 & Collins, W. (2016). Application of Deep Convolutional Neural Networks for Detecting
910 Extreme Weather in Climate Datasets. In arXiv [cs.CV]. arXiv.
911 <http://arxiv.org/abs/1605.01156>
- 912 Mamalakis, A., Ebert-Uphoff, I., & Barnes, E. A. (2022). Neural network attribution methods for
913 problems in geoscience: A novel synthetic benchmark dataset. *Environmental Data*
914 *Science*, 1, e8. <https://doi.org/10.1017/eds.2022.7>
- 915 McGovern, A., Lagerquist, R., Gagne, D. J., Eli Jergensen, G., Elmore, K. L., Homeyer, C. R., &
916 Smith, T. (2019). Making the Black Box More Transparent: Understanding the Physical
917 Implications of Machine Learning. *Bulletin of the American Meteorological Society*,
918 100(11), 2175–2199. <https://doi.org/10.1175/BAMS-D-18-0195.1>
- 919 Mei, R., & Wang, G. (2012). Summer Land–Atmosphere Coupling Strength in the United States:
920 Comparison among Observations, Reanalysis Data, and Numerical Models. *Journal of*
921 *Hydrometeorology*, 13(3), 1010–1022. <https://doi.org/10.1175/JHM-D-11-075.1>
- 922 Menéndez, Claudio G., Julián Giles, Romina Ruscica, Pablo Zaninelli, Tanea Coronato,
923 Magdalena Falco, Anna Sörensson, Lluís Fita, Andrea Carril, and Laurent Li. (2019).
924 “Temperature Variability and Soil–atmosphere Interaction in South America Simulated
925 by Two Regional Climate Models.” *Climate Dynamics* 53 (5): 2919–30.
- 926 Miralles, D. G., Teuling, A. J., van Heerwaarden, C. C., & Vilà-Guerau de Arellano, J. (2014).
927 Mega-heatwave temperatures due to combined soil desiccation and atmospheric heat
928 accumulation. *Nature Geoscience*, 7(5), 345–349. <https://doi.org/10.1038/ngeo2141>
- 929 Miralles, D. G., van den Berg, M. J., Teuling, A. J., & de Jeu, R. A. M. (2012). Soil moisture-
930 temperature coupling: A multiscale observational analysis. *Geophysical Research Letters*,
931 39(21). <https://doi.org/10.1029/2012gl053703>
- 932 Muñoz-Sabater, J., Dutra, E., Agustí-Panareda, A., Albergel, C., Arduini, G., Balsamo, G.,
933 Boussetta, S., Choulga, M., Harrigan, S., Hersbach, H., Martens, B., Miralles, D. G.,
934 Piles, M., Rodríguez-Fernández, N. J., Zsoter, E., Buontempo, C., & Jean-Noël Thépaut.
935 (2021). ERA5-Land: a state-of-the-art global reanalysis dataset for land applications.
936 [Dataset]. *Earth System Science Data*, 13(9), 4349–4383. [https://doi.org/10.5194/essd-](https://doi.org/10.5194/essd-13-4349-2021)
937 [13-4349-2021](https://doi.org/10.5194/essd-13-4349-2021)
- 938 Olah, C., Mordvintsev, A., & Schubert, L. (2017). Feature Visualization. *Distill*, 2(11).
939 <https://doi.org/10.23915/distill.00007>
- 940 Orth, R., & Seneviratne, S. I. (2012). Analysis of soil moisture memory from observations in
941 Europe. *Journal of Geophysical Research*. <https://doi.org/10.1029/2011JD017366>
- 942 Pan, B., Hsu, K., AghaKouchak, A., & Sorooshian, S. (2019). Improving precipitation estimation
943 using convolutional neural network. *Water Resources Research*, 55(3), 2301–2321.
944 <https://doi.org/10.1029/2018wr024090>
- 945 Pedregosa, F., Varoquaux, G., Gramfort, A., Michel, V., Thirion, B., Grisel, O., Blondel, M.,
946 Prettenhofer, P., Weiss, R., Dubourg, V., & Others. (2011). Scikit-learn: Machine
947 learning in Python. *The Journal of Machine Learning Research*, 12, 2825–2830.

- 948 <https://www.jmlr.org/papers/volume12/pedregosa11a/pedregosa11a.pdf?ref=https://githubhelp.com>
- 949
- 950 Quesada, B., Vautard, R., Yiou, P., Hirschi, M., & Seneviratne, S. I. (2012). Asymmetric
- 951 European summer heat predictability from wet and dry southern winters and springs.
- 952 *Nature Climate Change*, 2(10), 736–741. <https://doi.org/10.1038/nclimate1536>
- 953 Ruscica, R. C., Sörensson, A. A., & Menéndez, C. G. (2014). Hydrological links in Southeastern
- 954 South America: soil moisture memory and coupling within a hot spot. *International*
- 955 *Journal of Climatology*, 34(14), 3641–3653. <https://doi.org/10.1002/joc.3930>
- 956 Ryu, Y., Baldocchi, D. D., Ma, S., & Hehn, T. (2008). Interannual variability of
- 957 evapotranspiration and energy exchange over an annual grassland in California. *Journal*
- 958 *of Geophysical Research, D: Atmospheres*, 113(D9).
- 959 <https://doi.org/10.1029/2007JD009263>
- 960 Schwingshackl, C., Hirschi, M., & Seneviratne, S. I. (2017). Quantifying Spatiotemporal
- 961 Variations of Soil Moisture Control on Surface Energy Balance and Near-Surface Air
- 962 Temperature. *Journal of Climate*, 30(18), 7105–7124. [https://doi.org/10.1175/JCLI-D-16-](https://doi.org/10.1175/JCLI-D-16-0727.1)
- 963 [0727.1](https://doi.org/10.1175/JCLI-D-16-0727.1)
- 964 Schwingshackl, C., Hirschi, M., & Seneviratne, S. I. (2018). A theoretical approach to assess soil
- 965 moisture–climate coupling across CMIP5 and GLACE-CMIP5 experiments. *Earth*
- 966 *System Dynamics Discussions*, 1–26. <https://doi.org/10.5194/esd-2018-34>
- 967 Seneviratne, S. I., Corti, T., Davin, E. L., Hirschi, M., Jaeger, E. B., Lehner, I., Orlowsky, B., &
- 968 Teuling, A. J. (2010). Investigating soil moisture–climate interactions in a changing
- 969 climate: A review. *Earth-Science Reviews*, 99(3), 125–161.
- 970 <https://doi.org/10.1016/j.earscirev.2010.02.004>
- 971 Seneviratne, S. I., Koster, R. D., Guo, Z., Dirmeyer, P. A., Kowalczyk, E., Lawrence, D., Liu, P.,
- 972 Mocko, D., Lu, C.-H., Oleson, K. W., & Verseghy, D. (2006). Soil Moisture Memory in
- 973 AGCM Simulations: Analysis of Global Land–Atmosphere Coupling Experiment
- 974 (GLACE) Data. *Journal of Hydrometeorology*, 7(5), 1090–1112.
- 975 <https://doi.org/10.1175/JHM533.1>
- 976 Seneviratne, S. I., Lüthi, D., Litschi, M., & Schär, C. (2006). Land–atmosphere coupling and
- 977 climate change in Europe. *Nature*, 443(7108), 205–209.
- 978 <https://doi.org/10.1038/nature05095>
- 979 Seneviratne, S. I., Wilhelm, M., Stanelle, T., Hurk, B., Hagemann, S., Berg, A., Cheruy, F.,
- 980 Higgins, M. E., Meier, A., Brovkin, V., Claussen, M., Ducharne, A., Dufresne, J.-L.,
- 981 Findell, K. L., Ghattas, J., Lawrence, D. M., Malyshev, S., Rummukainen, M., & Smith,
- 982 B. (2013). Impact of soil moisture–climate feedbacks on CMIP5 projections: First results
- 983 from the GLACE-CMIP5 experiment. *Geophysical Research Letters*, 40(19), 5212–5217.
- 984 <https://doi.org/10.1002/grl.50956>
- 985 Shukla, J., & Mintz, Y. (1982). Influence of Land-Surface Evapotranspiration on the Earth’s
- 986 Climate. *Science*, 215(4539), 1498–1501. <https://doi.org/10.1126/science.215.4539.1498>
- 987 Song, Y. M., Wang, Z. F., Qi, L. L., & Huang, A. N. (2019). Soil moisture memory and its effect
- 988 on the surface water and heat fluxes on seasonal and interannual time scales. *Journal of*
- 989 *Geophysical Research*, 124(20), 10730–10741. <https://doi.org/10.1029/2019jd030893>
- 990 Spennemann, P. C., M. Salvia, R. C. Ruscica, A. A. Sörensson, F. Grings, and H. Karszenbaum.
- 991 (2018). “Land-Atmosphere Interaction Patterns in Southeastern South America Using
- 992 Satellite Products and Climate Models.” *International Journal of Applied Earth*
- 993 *Observation and Geoinformation* 64 (February): 96–103.

- 994 Steininger, M., Kobs, K., Davidson, P., Krause, A., & Hotho, A. (2021). Density-based
 995 weighting for imbalanced regression. *Machine Learning*, 110(8), 2187–2211.
 996 <https://doi.org/10.1007/s10994-021-06023-5>
- 997 Swain, D. L., Horton, D. E., Singh, D., & Diffenbaugh, N. S. (2016). Trends in atmospheric
 998 patterns conducive to seasonal precipitation and temperature extremes in California.
 999 *Science Advances*, 2(4), e1501344. <https://doi.org/10.1126/sciadv.1501344>
- 1000 Teuling, A. J., Hirschi, M., Ohmura, A., Wild, M., Reichstein, M., Ciais, P., Buchmann, N.,
 1001 Ammann, C., Montagnani, L., Richardson, A. D., Wohlfahrt, G., & Seneviratne, S. I.
 1002 (2009). A regional perspective on trends in continental evaporation. *Geophysical*
 1003 *Research Letters*, 36(2). <https://doi.org/10.1029/2008gl036584>
- 1004 Toms, B. A., Barnes, E. A., & Ebert-Uphoff, I. (2020). Physically interpretable neural networks
 1005 for the geosciences: Applications to earth system variability. *Journal of Advances in*
 1006 *Modeling Earth Systems*, 12(9). <https://doi.org/10.1029/2019ms002002>
- 1007 Vautard, R., Yiou, P., D’Andrea, F., de Noblet, N., Viovy, N., Cassou, C., Polcher, J., Ciais, P.,
 1008 Kageyama, M., & Fan, Y. (2007). Summertime European heat and drought waves
 1009 induced by wintertime Mediterranean rainfall deficit. *Geophysical Research Letters*,
 1010 34(7). <https://doi.org/10.1029/2006GL028001>
- 1011 Vogel, M. M., R. Orth, F. Cheruy, S. Hagemann, R. Lorenz, B. J. J. M. van den Hurk, and S. I.
 1012 Seneviratne. (2017). “Regional Amplification of Projected Changes in Extreme
 1013 Temperatures Strongly Controlled by Soil Moisture-Temperature Feedbacks.”
 1014 *Geophysical Research Letters* 44 (3): 1511–19.
- 1015 Wang, L., Scott, K. A., Xu, L., & Clausi, D. A. (2016). Sea Ice Concentration Estimation During
 1016 Melt From Dual-Pol SAR Scenes Using Deep Convolutional Neural Networks: A Case
 1017 Study. *IEEE Transactions on Geoscience and Remote Sensing: A Publication of the IEEE*
 1018 *Geoscience and Remote Sensing Society*, 54(8), 4524–4533.
 1019 <https://doi.org/10.1109/TGRS.2016.2543660>
- 1020 Wickham, H., Cook, D., Hofmann, H., & Buja, A. (2010). Graphical inference for Infovis. *IEEE*
 1021 *Transactions on Visualization and Computer Graphics*, 16(6), 973–979.
 1022 <https://doi.org/10.1109/TVCG.2010.161>
- 1023 Wimmers, A., Velden, C., & Cossuth, J. H. (2019). Using Deep Learning to Estimate Tropical
 1024 Cyclone Intensity from Satellite Passive Microwave Imagery. *Monthly Weather Review*,
 1025 147(6), 2261–2282. <https://doi.org/10.1175/MWR-D-18-0391.1>
- 1026 Wu, W., & Dickinson, R. E. (2004). Time Scales of Layered Soil Moisture Memory in the
 1027 Context of Land–Atmosphere Interaction. *Journal of Climate*, 17(14), 2752–2764.
 1028 [https://doi.org/10.1175/1520-0442\(2004\)017<2752:TSOLSM>2.0.CO;2](https://doi.org/10.1175/1520-0442(2004)017<2752:TSOLSM>2.0.CO;2)
- 1029 Zender, C. S. (2008). Analysis of self-describing gridded geoscience data with netCDF Operators
 1030 (NCO). *Environmental Modelling & Software*, 23(10), 1338–1342.
 1031 <https://doi.org/10.1016/j.envsoft.2008.03.004>
- 1032 Zhang, G., Wang, M., & Liu, K. (2021). Deep neural networks for global wildfire susceptibility
 1033 modelling. *Ecological Indicators*, 127, 107735.
 1034 <https://doi.org/10.1016/j.ecolind.2021.107735>

Using Machine Learning with Partial Dependence Analysis to Investigate Coupling Between Soil Moisture and Near-surface Temperature

Jared T. Trok¹, Frances V. Davenport^{1,2,3}, Elizabeth A. Barnes², and Noah S. Diffenbaugh^{1,4}

¹Department of Earth System Science, Stanford University, Stanford, CA, USA. ²Department of Atmospheric Science, Colorado State University, Fort Collins, CO, USA. ³Department of Civil and Environmental Engineering, Colorado State University, Fort Collins, CO, USA. ⁴Doerr School of Sustainability, Stanford University, Stanford, CA, USA.

Contents of this file

Figures S1 to S11

Introduction

The following document consists of four figures (S1-S4) supporting our primary analysis (using the 1979-2021 ERA5 and ERA5-Land historical reanalysis datasets), and seven figures (S5-S11) showing the results of our secondary analysis (using the 1979-2021 NCEP/DOE R2 historical reanalysis dataset). Figure S1 compares the mean seasonal cycle of daily maximum 2-meter temperature (TMAX) between the ERA5 dataset and convolutional neural network (CNN) predictions. Figure S2 shows each CNN's ability to predict daily TMAX anomalies from the seasonal cycle. Figure S3 shows subregional variability in soil moisture-temperature relationships obtained through partial dependence analysis (using southcentral North America as an example). Figure S4 provides examples of regional soil moisture-temperature relationships obtained through partial dependence analysis of CNNs trained using datasets with randomly shuffled soil moisture input maps. Figures S5 through S11 present the results of our analysis when applied to the NCEP/DOE R2 historical reanalysis dataset (1979-2021).

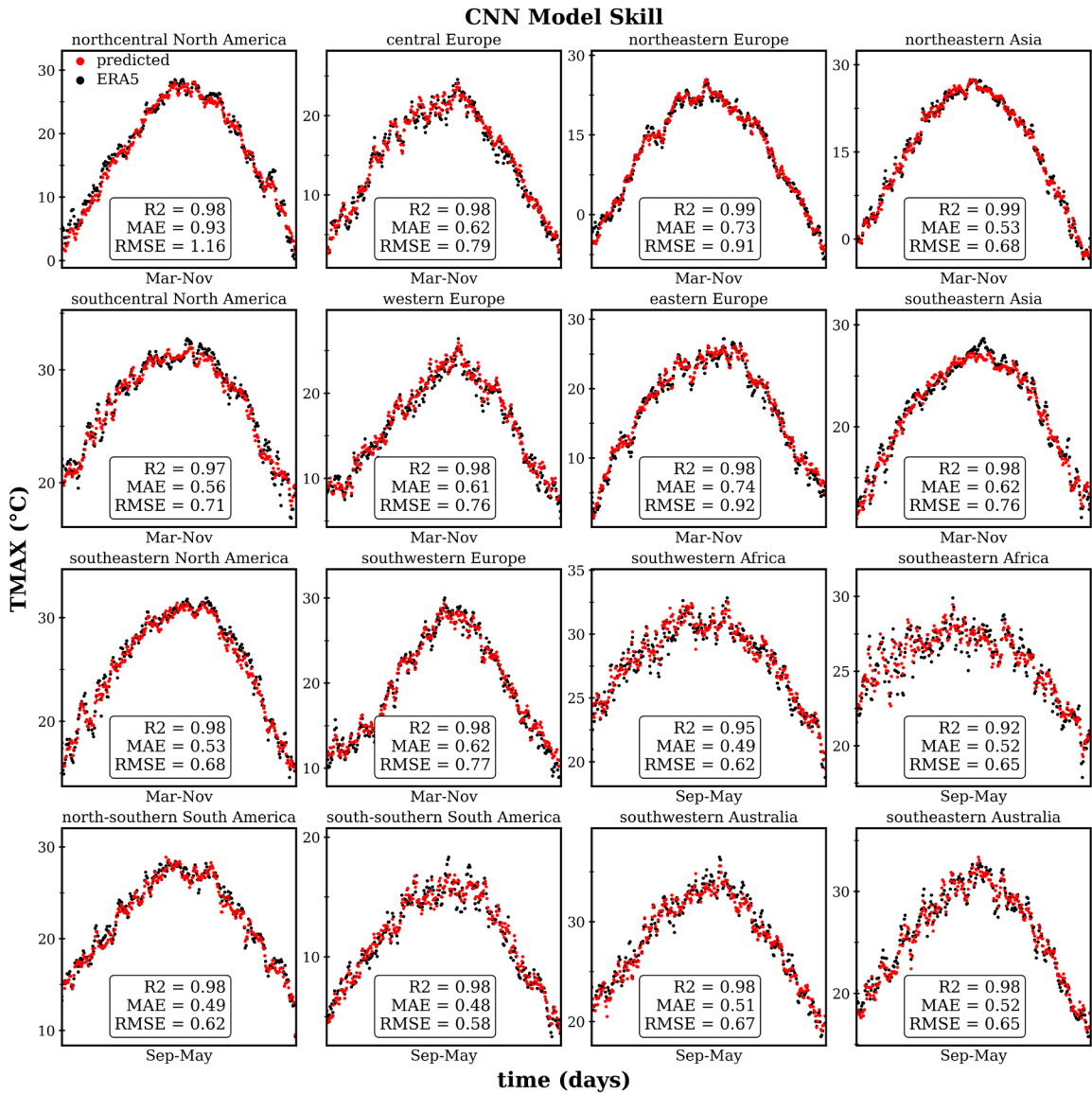


Figure S1. Comparison of the annual temperature cycle between (black) ERA5-Land daily maximum 2-meter temperatures (TMAX) and (red) convolutional neural network TMAX predictions. Each subplot shows the mean seasonal cycle of TMAX over snow-free months averaged across all 8 years in the testing subset. The coefficient of determination (R2), mean absolute error (MAE), and mean squared error (MSE) is shown for each region. Snow-free months are defined as March-November (Mar-Nov) in the Northern Hemisphere and September-May (Sep-May) in the Southern Hemisphere.

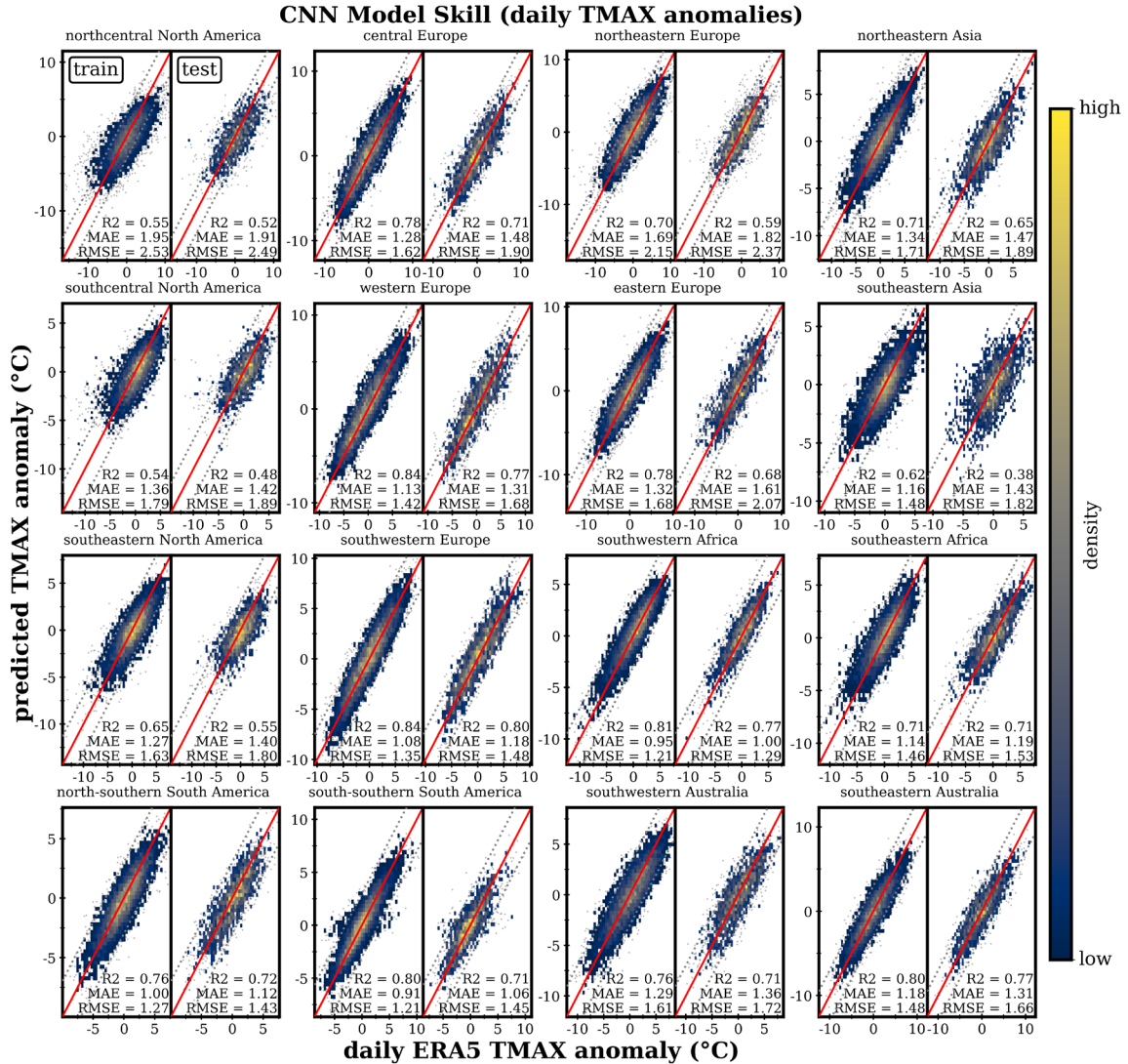


Figure S2. Comparison between model predicted temperature anomaly and ERA5-Land temperature anomaly for each convolutional neural network trained to predict daily maximum 2-meter temperature (TMAX) over a region. Each regional subplot shows the coefficient of determination (R2), mean absolute error (MAE), and mean squared error (MSE) for both the training dataset (left) and the testing dataset (right). Daily TMAX anomalies calculated as deviations from the ERA5 seasonal cycle (see Figure S1). Correct predictions fall along the 1-1 line (red). Gray dotted lines show +/- 3 degrees C prediction errors.

Subregional variability in SM-T Partial Dependence Plots

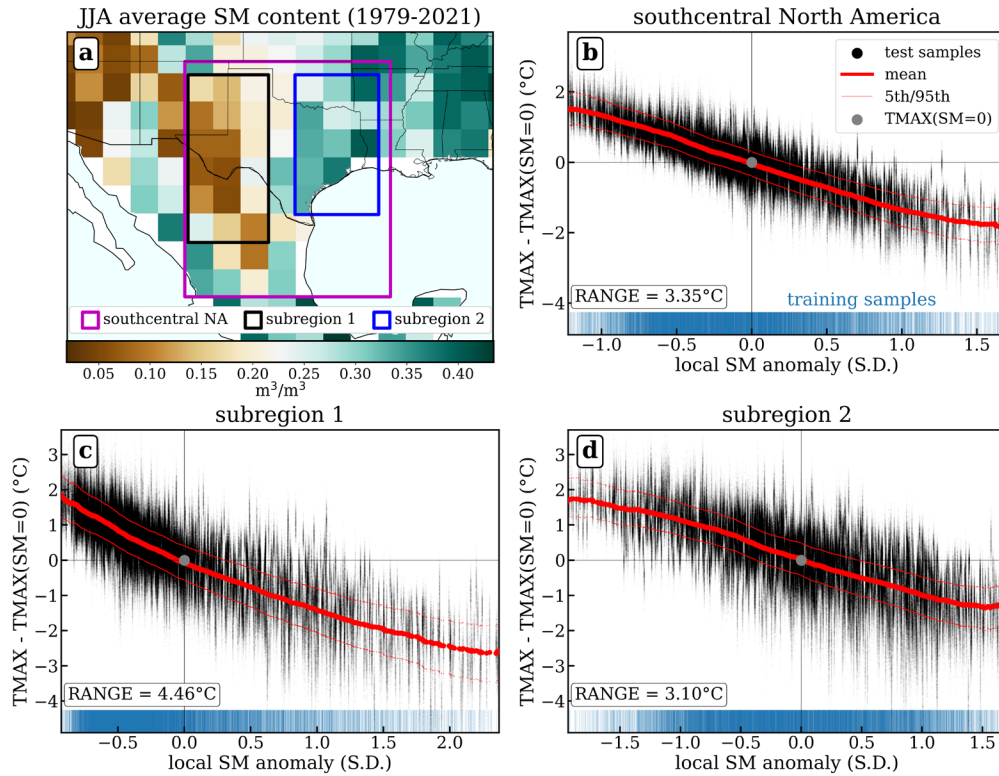


Figure S3. Subregional variability in soil moisture-temperature (SM-T) relationships obtained through partial dependence analysis (method detailed in Figure 2) of convolutional neural networks. (a) Average summertime (June-August) SM content over southcentral North America and two subregions which exhibit dry (subregion 1) and wet (subregion 2) summertime SM conditions, respectively. (b, c, d) SM-T relationships calculated from CNNs trained to predict TMAX over (b) southcentral North America (reproduced from Figure 7), (c) subregion 1, and (d) subregion 2. The smoothed moving average (thick red line) shows the average behavior of the neural network's TMAX prediction as the SM input varies from dry (negative) to wet (positive) local SM anomalies. Also shown are the moving 5th and 95th percentiles of the temperature predictions (thin red lines). The SM-T relationships shown are calculated from the testing dataset. We also include a rug plot showing the distribution of SM anomalies in the training dataset. For each region and subregion, we calculate the range (vertical extent) of the mean SM-T relationship. The local soil moisture anomalies (x-axis) are calculated as standard deviations (S.D.) from the calendar-day mean and averaged over all non-ocean grid cells within the region bounds.

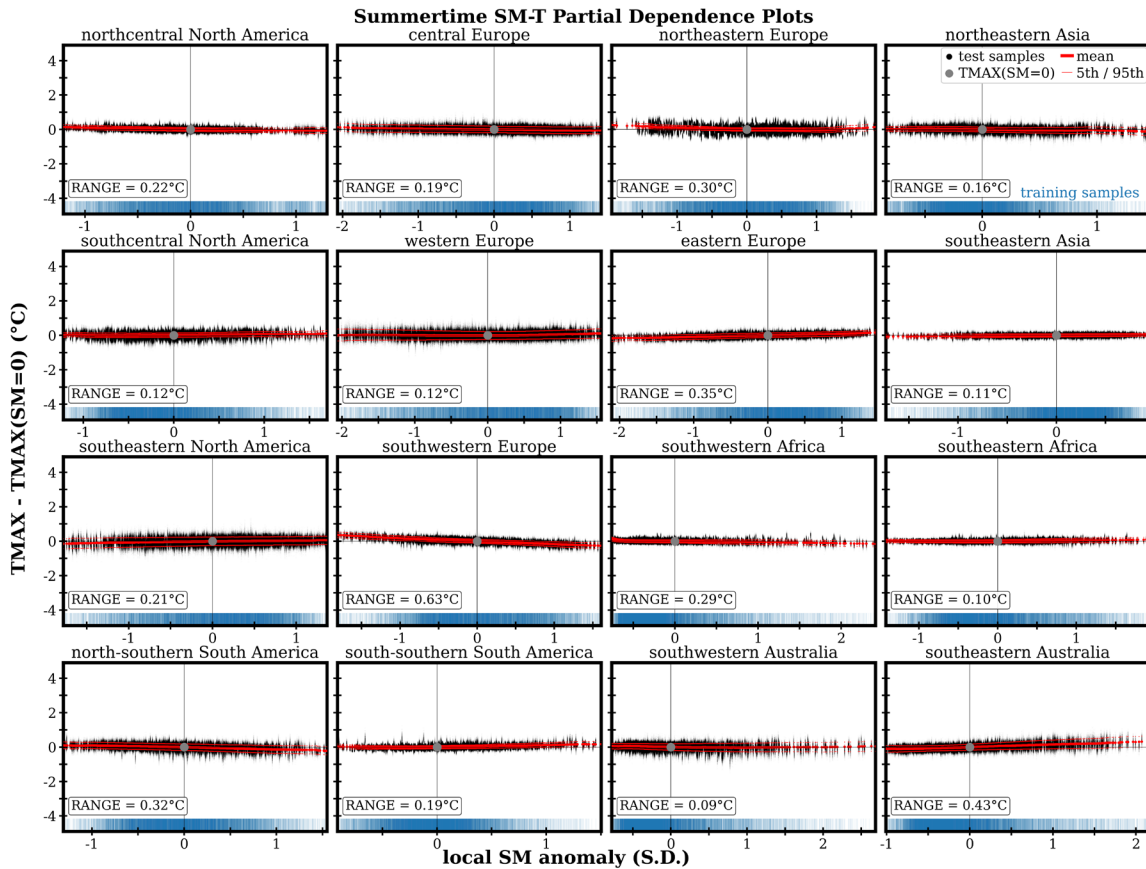


Figure S4. Soil moisture-temperature (SM-T) relationships obtained through partial dependence analysis (method detailed in Figure 2) of convolutional neural networks trained with randomly shuffled soil moisture input maps. The smoothed moving average (thick red line) shows the average behavior of the neural network's prediction as the SM input varies from dry (negative) to wet (positive) local SM anomalies. Also shown are the moving 5th and 95th percentiles of the temperature predictions (thin red lines). The SM-T relationships shown are calculated from the testing dataset. We also include a rug plot showing the distribution of SM anomalies in the training dataset. For each subplot, we calculate the range (vertical extent) of the mean SM-T relationship. Soil moisture anomalies are calculated as standard deviations (S.D.) from the calendar-day mean.

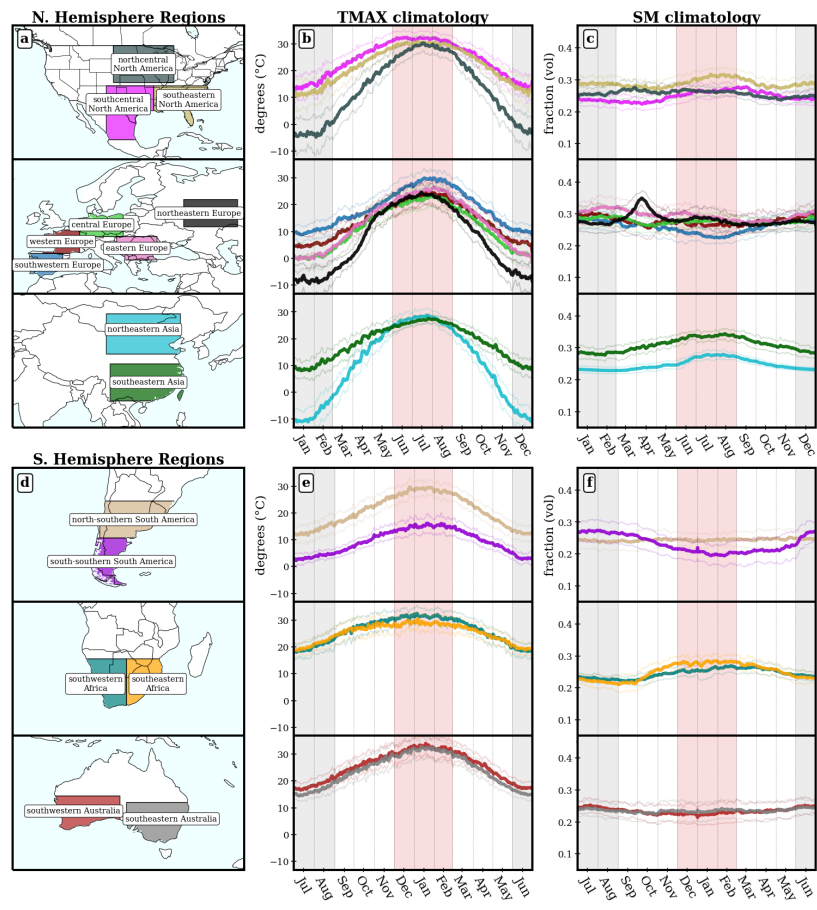


Figure S5. Same as Figure 3, except climatologies are calculated using the 1979-2021 NCEP/DOE R2 (NCEP) reanalysis dataset. (a) Northern Hemisphere regions included in this analysis alongside 1979-2021 regional climatologies of (b) daily maximum 2-meter temperature (TMAX), and (c) volumetric soil moisture fraction (SM). Thin lines show +/- 1 standard deviation from climatological mean. (d, e, f) Same as (a, b, c) but for Southern Hemisphere regions. Red shading indicates summer months in each hemisphere over which this study analyzes soil moisture-temperature coupling. Gray shading indicates winter months removed from all subsequent analyses.

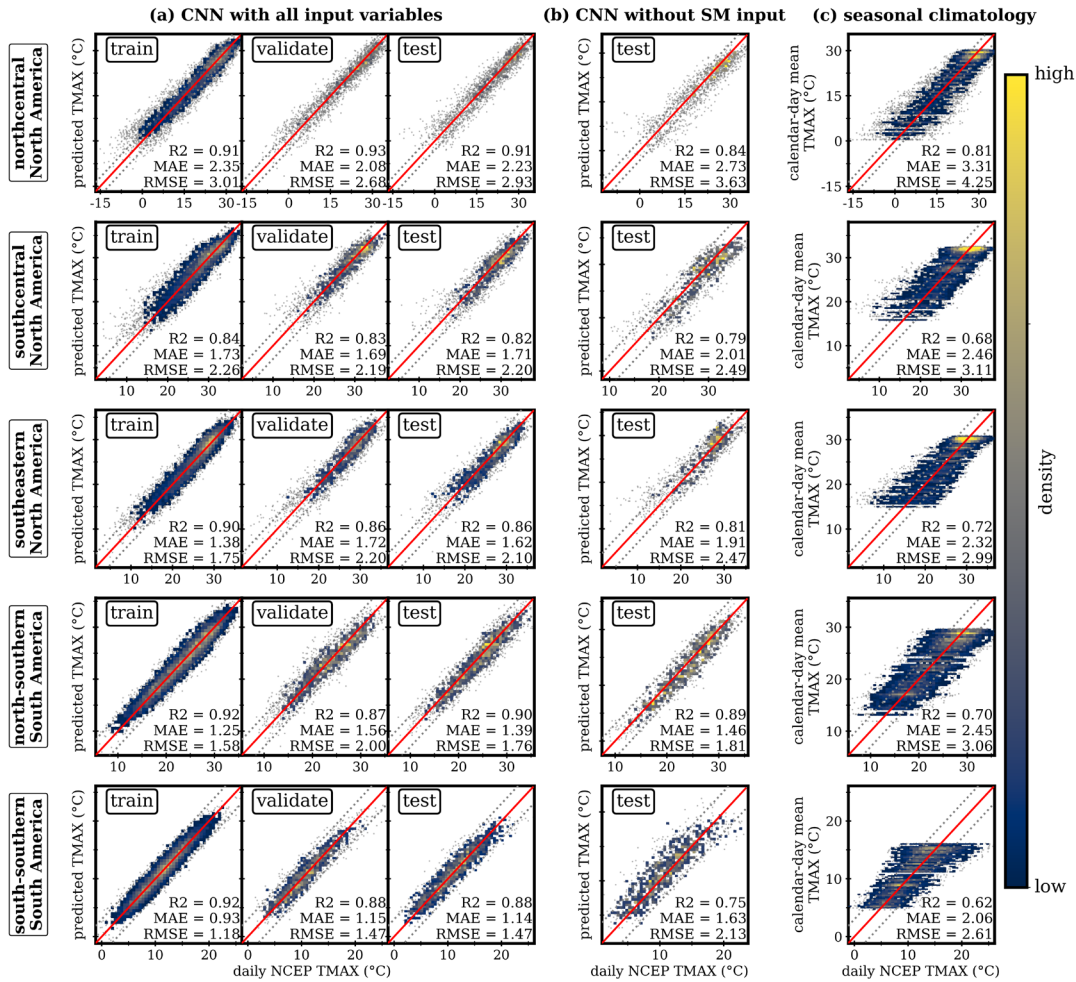


Figure S6. Same as Figure 4, but for convolutional neural networks trained using the 1979-2021 NCEP/DOE R2 (NCEP) reanalysis dataset. CNN model skill comparison for North and South American regions. (a) Comparison between ERA5-Land TMAX and predicted TMAX from convolutional neural networks (CNNs) trained with daily geopotential height anomaly maps, soil moisture anomaly maps (SM), and normalized calendar day inputs. Model performance is shown separately for the 27-year training subset (used to fit CNN weights), the 8-year validation subset (used to optimize hyperparameters), and the 8-year testing subset (unseen data left out of the training process). See Methods for more details on the training, validation, and testing subsets. (b) Same as (a) but for CNNs trained without the SM inputs. Model performance is shown for the 8-year testing subset. (c) The seasonal climatology of TMAX as shown by comparing the ERA5-Land daily TMAX and the calendar-day mean TMAX each day (averaged over 1979-2021). Each subplot shows the coefficient of determination (R^2), mean absolute error (MAE), and mean squared error (MSE). Correct predictions fall along the 1-1 line (red). Gray dotted lines show ± 3 degrees C prediction errors.

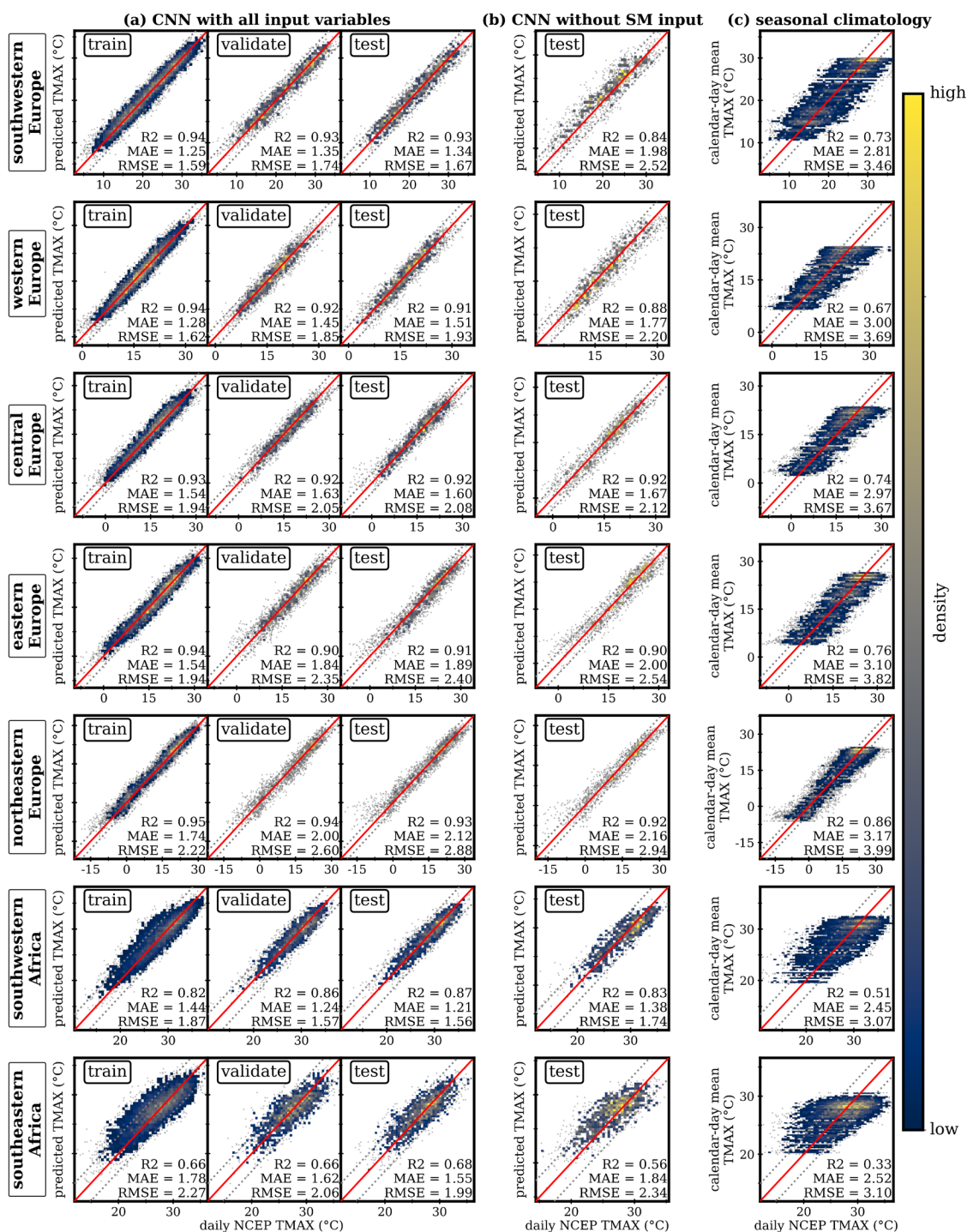


Figure S7. Same as Figure 5, but for convolutional neural networks trained using the 1979-2021 NCEP/DOE R2 (NCEP) reanalysis dataset. CNN model skill comparison for regions in Europe and Africa.

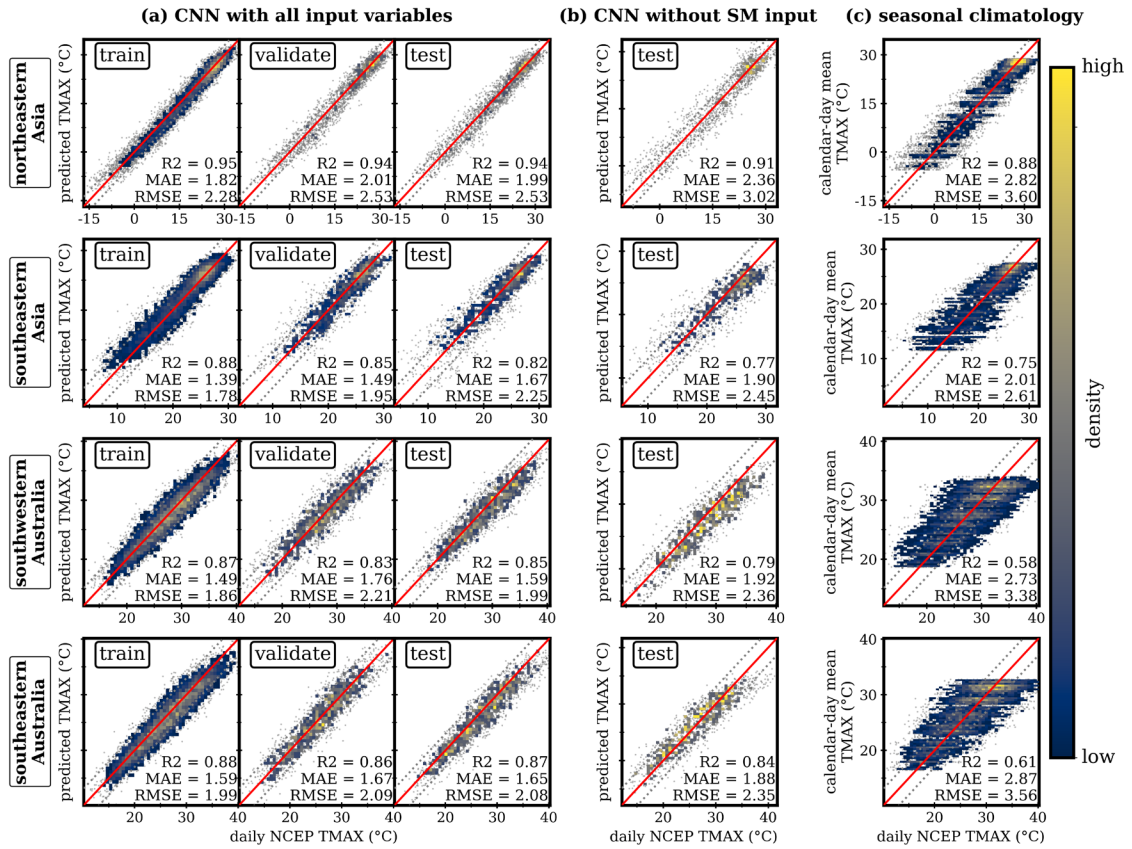


Figure S8. Same as Figure 6, but for convolutional neural networks trained using the 1979-2021 NCEP/DOE R2 (NCEP) reanalysis dataset. CNN model skill comparison for regions in Eastern Asia and Australia.

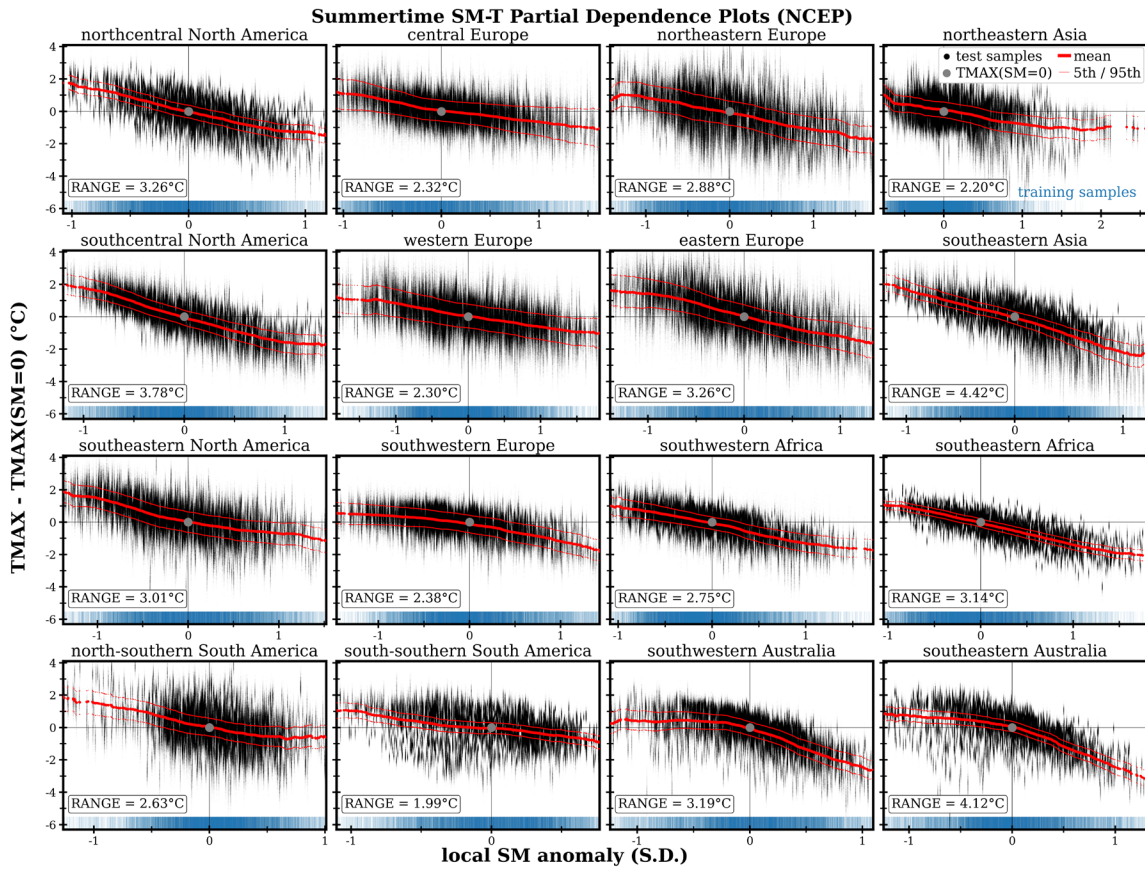


Figure S9. Same as Figure 7, but for convolutional neural networks trained using the 1979-2021 NCEP/DOE R2 (NCEP) reanalysis dataset. Soil moisture-temperature (SM-T) relationships obtained through partial dependence analysis of convolutional neural networks (method detailed in Figure 2). The smoothed moving average (thick red line) shows the average behavior of the neural network's prediction as the SM input varies from dry (negative) to wet (positive) anomalies. Also shown are the moving 5th and 95th percentiles of the temperature predictions (thin red lines). The SM-T relationships shown are calculated from the testing dataset. We also include a rug plot showing the distribution of SM anomalies in the training dataset. For each subplot, we calculate the range (vertical extent) of the mean SM-T relationship. Soil moisture anomalies are calculated as standard deviations (S.D.) from the calendar-day mean.

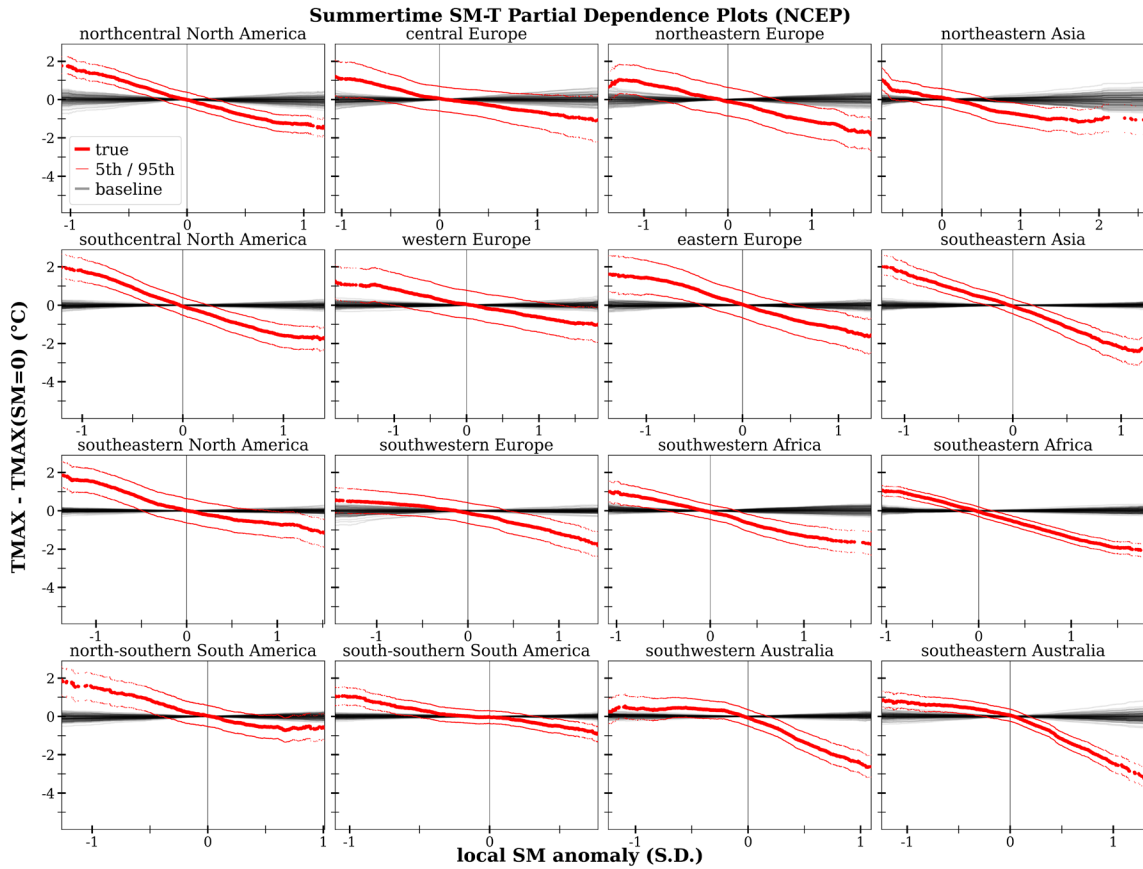


Figure S10. Same as Figure 8, but for convolutional neural networks trained using the 1979-2021 NCEP/DOE R2 (NCEP) reanalysis dataset. Regional soil moisture-temperature (SM-T) relationships obtained through partial dependence analysis (method detailed in Figure 2) of convolutional neural networks (CNNs) trained to predict regional daily maximum temperature (TMAX) given geopotential height, calendar-day, and soil moisture inputs. Each regional subplot shows 101 SM-T partial dependence plots (PDPs), consisting of the true SM-T PDP (red; Figure 7) and 100 baseline SM-T PDPs (black) derived from CNNs trained with shuffled soil moisture inputs (each shuffled using a different random seed). Also shown are the moving 5th and 95th percentiles of the true SM-T PDP (thin red lines). Soil moisture anomalies are calculated as standard deviations (S.D.) from the calendar-day mean.

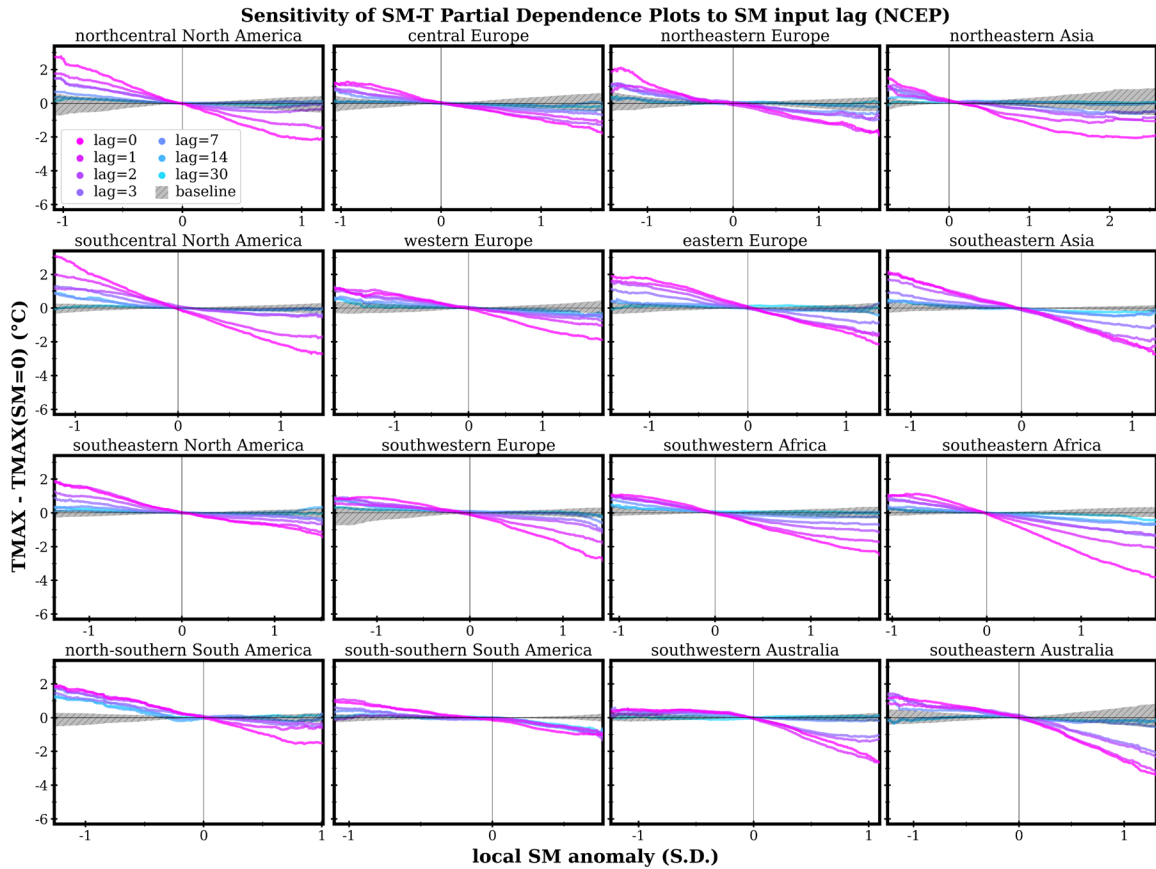


Figure S11. Same as Figure 9, but for convolutional neural networks trained using the 1979-2021 NCEP/DOE R2 (NCEP) reanalysis dataset. Regional soil moisture-temperature (SM-T) partial dependence relationships obtained using the method detailed in Figure 2 (but for CNNs trained with various levels of soil moisture input lag). Each regional subplot shows SM-T relationships derived from 7 different CNNs trained to predict daily TMAX given the following inputs: calendar day, daily GPH anomaly map, and a single day's SM anomaly map lagged by 0-30 days prior to the prediction day. After the training process, CNN weights are saved and used to calculate the SM-T PDPs as in Figure 2. Colors show SM-T relationships for CNNs trained with SM input lags of 0, 1, 2, 3, 7, 14, and 30 days. Hatching shows the range of the 100 baseline PDPs (Figure 8). Soil moisture anomalies are calculated as standard deviations (S.D.) from the calendar-day mean.